1   **Spatio-temporal Control of ERK Pulse Frequency Coordinates Fate Decisions**

2   **during Mammary Acinar Morphogenesis**

3

4   Pascal Ender [1,2], Paolo Armando Gagliardi [1], Maciej Dobrzyński [1], Agne Frismantiene

5   [1], Coralie Dessauges [1], Thomas Höhener [1], Marc-Antoine Jacques [1,3], Andrew R.

6   Cohen [4], and Olivier Pertz [1]*

7   1 Institute of Cell Biology, University of Bern, Baltzerstrasse 4, 3012 Bern, Switzerland

8   2 present address: Department of Autonomous Matter, AMOLF, Science Park 104,

9   1098 XG Amsterdam, The Netherlands

10   3 present addresses: Cancer Research UK Cambridge Institute, University of

11   Cambridge, Li Ka Shing Centre, Robinson Way, Cambridge, CB2 0RE, United

12   Kingdom; and, Wellcome Genome Campus, Hinxton, Cambridgeshire, CB10 1SD,

13   United Kingdom

14   4 Department of Electrical and Computer Engineering, Drexel University, 3120-40

15   Market Street, Suite 313, Philadelphia, PA 19104, USA

16   *Correspondence and requests for materials should be addressed to O.P. (email:

17   olivier.pertz@unibe.ch).

Abstract

The signaling events controlling proliferation, survival, and apoptosis during mammary epithelial acinar morphogenesis remain poorly characterized. By imaging single-cell ERK activity dynamics in MCF10A acini, we find that these fates depend on the average frequency of non-periodic ERK pulses. High pulse frequency is observed during initial acinus growth, correlating with rapid cell motility. Subsequent decrease in motility correlates with lower ERK pulse frequency and quiescence. Later, during lumen formation, coordinated ERK waves emerge across multiple cells of an acinus, correlating with high and low ERK pulse frequency in outer surviving and inner dying cells respectively. Optogenetic entrainment of ERK pulses causally connects high ERK pulse frequency with inner cell survival. Acini harboring the PIK3CA H1047R mutation, commonly observed in breast cancer, display increased ERK pulse frequency, inner cell survival and loss of lumen formation. Thus, fate decisions during acinar morphogenesis are fine-tuned by different spatio-temporal coordination modalities of ERK pulse frequency.

Introduction

33

34 Mammary organogenesis involves formation of a rudimentary gland during
35 embryogenesis, followed by proliferation and branching invasion led by multi-layered
36 terminal end buds (TEBs) during puberty. Cells in the inner TEB layers then undergo
37 apoptosis to form the ductal lumen. During pregnancy, secretory alveoli are then
38 formed at the ends of the ductal tree (Inman et al., 2015; Paine and Lewis, 2017).
39 Morphogenesis of this complex structure requires spatial and temporal control of cell
40 fates such as proliferation, survival, migration and death. However, the spatio-
41 temporal signaling events that regulate such fate decisions remain poorly explored.
42 The epidermal growth factor (EGF) receptor (EGFR) – mitogen activated protein
43 kinase (MAPK) signaling cascade, that ultimately leads to activation of the extracellular
44 regulated kinase (ERK) is a key pathway involved in mammary gland development.
45 EGFR-ERK signaling results in the upregulation of gene products involved in a wide
46 variety of processes such as proliferation, survival, migration and differentiation
47 (Lavoie et al., 2020). EGFR activity is required for mammary gland morphogenesis in
48 mice (Sebastian et al., 1998). Paracrine amphiregulin release by the matrix metallo-
49 protease (MMP) ADAM-17 and its binding to EGFR mediates the effects of estrogen
50 receptor α to promote mammary gland development and growth (Ciarloni et al., 2007;
51 Sternlicht et al., 2005). EGFR-dependent ERK activity is enriched at the front of
52 elongating tubes and coordinates cell migration (Huebner et al., 2016). In 3D
53 mammary acini, oncogenic ERK activation suppresses apoptosis and thus lumen
54 formation (Reginato et al., 2005). In primary mammary cell culture, ERK activity is
55 also crucial for survival (Finlay et al., 2000).

56 Recent single-cell measurements of ERK activity dynamics in a variety of 2D epithelial
57 monolayer cultures have revealed the existence of non-periodic ERK pulses of
58 constant amplitude and duration (Aikin et al., 2020; Albeck et al., 2013; Aoki et al.,
59 2013; Gagliardi et al., 2021; Goglia et al., 2020; Hino et al., 2020; Hiratsuka et al.,
60 2015). These ERK pulses originate from MAPK network properties such as
61 ultrasensitivity (leading to steep ERK activation at a threshold EGFR input), and
62 negative feedback (leading to ERK adaptation) (Kholodenko et al., 2010; Sparta et al.,
63 2015). An emerging theme is that the average frequency of these non-periodic ERK
64 pulses, referred to as ERK frequency from now on, control apoptosis (low frequency),
65 survival (medium frequency) or proliferation (high frequency) (Albeck et al., 2013; Aoki
66 et al., 2013; Gagliardi et al., 2021). These ERK pulses can either exhibit a stochastic

3

67 spatially uncorrelated behavior (Albeck et al., 2013; Goglia et al., 2020), or can be
68 organized as wave patterns that regulate collective cell migration in a wound (Aoki et
69 al., 2017; Hino et al., 2020; Hiratsuka et al., 2015), cell survival around sites of
70 apoptotic cell extrusion (Gagliardi et al., 2021; Valon et al., 2021), or extrusion of
71 cancer cells (Aikin et al., 2020). These ERK signaling patterns consist of trigger waves
72 that involve sequential activation of ERK pulses in adjacent epithelial cells through
73 paracrine signaling involving MMP-mediated cleavage of pro-EGF ligands.

74 In this work, we explore single cell ERK dynamics in 3D mammary acini. Culturing
75 mammary MCF10A cells in a basement membrane matrix (Matrigel) produces acini
76 that retain key features of in vivo breast alveoli. Based on previous work (Anderson et
77 al., 2010; Debnath et al., 2003), we subdivided this process into four stages as
78 depicted in Figure S1A. Stage 1 is characterized by high proliferation rates and
79 basement membrane deposition; stage 2 consists of a quiescent state and presence
80 of an outer cell layer with clear basolateral polarity; stage 3 consists of apoptosis of
81 inner cells that allows formation of a hollow lumen in stage 4. The whole process takes
82 approximately two weeks.

83 We document different spatio-temporal modalities of ERK signaling during different
84 developmental stages of MCF10A acini formation. Stage 1 is characterized by high
85 ERK frequency, robust proliferation and rapid collective motility. This is followed by a
86 transition to lower ERK frequency and slower collective motility. During stage 2,
87 formation of ERK wave patterns correlates with domains of different ERK frequencies:
88 outer/inner cells display medium/low ERK frequencies, respectively controlling
89 survival and apoptosis. Optogenetic control of ERK signaling shows that ERK pulses
90 control collective migration during stage 1, and that a critical ERK frequency is
91 necessary for survival during stage 2. We characterize a crosstalk between phospho-
92 inositide-3 kinase (PI3K) and MAPK/ERK signaling that feeds into the regulation of
93 ERK frequency. This provides insight into how oncogenic PI3K signaling crosstalks
94 with ERK to contribute to loss of lumen formation. Our work reveals how spatio-
95 temporal control of ERK frequency organizes mammary acinar morphogenesis.

96 **Results**

97 **Stage 1 proliferative acini exhibit non-periodic MMP/EGFR-dependent ERK pulses**

98 **whose frequency correlates with collective cell migration speed.**

99 To explore single-cell ERK dynamics during acinar morphogenesis, we created

100 MCF10A reporter lines expressing the nuclear marker histone 2B (H2B) fused to

101 miRFP703 with either the ERK activity biosensor ERK-KTR fused to mTurquoise2, or

102 a mCherry-geminin S/G2/M cell cycle marker (Sakaue-Sawano et al., 2017). ERK-

103 KTR reports on ERK activity through reversible nucleus/cytosol shuttling after its

104 phosphorylation by active ERK (Regot et al., 2014) (Figure 1A). These lines were then

105 used to grow acini according to a modified version of a previously described protocol

106 (Debnath et al., 2003). After three days, in which EGF, serum and insulin were required

107 for initial acinar growth, these growth factors (GFs) were removed to study ERK

108 signaling dynamics intrinsic to acinar morphogenesis. Using the geminin marker and

109 a fluorogenic caspase substrate, we evaluated if our protocol recapitulated the

110 proliferation, quiescence and apoptosis fates previously documented during acinar

111 morphogenesis (Figure S1B-E) (Debnath et al., 2002; Liu et al., 2012). Stage 1 acini

112 (4 days post-seeding) displayed elevated levels of proliferation and absence of

113 apoptosis. Stage 2 and 3 acini (7 and 11 days post-seeding) revealed quiescent cells

114 and increased apoptosis leading to lumen formation. Stage 4 acini (14 days post-

115 seeding) exhibited a mature lumen, abundant apoptotic debris, and a small increase

116 in proliferation.

117 We then imaged single-cell ERK dynamics in stage 1 acini using confocal spinning

118 disk microscopy of both the H2B and ERK-KTR channels with time resolutions of 3 -

119 5 minutes, until acini started to suffer from phototoxicity (observed after 10 - 23 hours).

120 Cells in stage 1 acini displayed asynchronous, non-periodic ERK pulses (Figure 1B)

121 as observed in 2D culture (Aikin et al., 2020; Albeck et al., 2013; Gagliardi et al., 2021).

122 To extract single-cell ERK activity trajectories, we used a customized version of the

123 open-source LEVERJS software (Wait et al., 2014; Winter et al., 2016) that segments

124 and tracks nuclei based on H2B signal; and calculates ERK activity as a ratio of ERK-

125 KTR fluorescence intensities in cytosolic and nuclear voxel masks (Figure 1C).

126 Detrending of the ERK trajectories and normalization of the values to [0,1] generated

127 a reliable input for automated detection of ERK pulses (Figure 1C). Single cell ERK

128 trajectories revealed spontaneous ERK pulses with slightly different amplitudes

129 (Figure 1D). Trametinib-mediated MEK, gefitinib-mediated EGFR, as well as

130   Batimastat-mediated MMP inhibition abolished ERK pulses (Figure 1E). MEK or EGFR

131   inhibition for multiple days led to massive cell death and disintegration of the acini

132   (Figure S2A), suggesting that ERK provides a pro-survival signal. Acute stimulation

133   with 1 ng/ml EGF induced ERK pulses of amplitudes similar to those of spontaneous

134   pulses, while 100 ng/ml EGF induced ERK pulses of higher amplitudes (Figure 1F,G).

135   These results document spontaneous, asynchronous EGFR- and MMP-depedent

136   ERK pulses in stage 1 acini.

137   As previously described (Wang et al., 2013), stage 1 acini displayed collective cell

138   motility correlating with a rotational movement of 360 degrees of whole acini over

139   multiple hours. Later during stage 1, we observed a transition to a state of slower

140   motility (Figure 2A, Movie S1). This was shown to correlate with deposition of

141   basement membrane around the acinus (Wang et al., 2013). The reduction in

142   migration speed correlated with decreased ERK frequency (Figure 2B-D and S3A,

143   Movie S2), without having a significant effect on ERK pulse amplitude and duration

144   (Figure S3B,C).
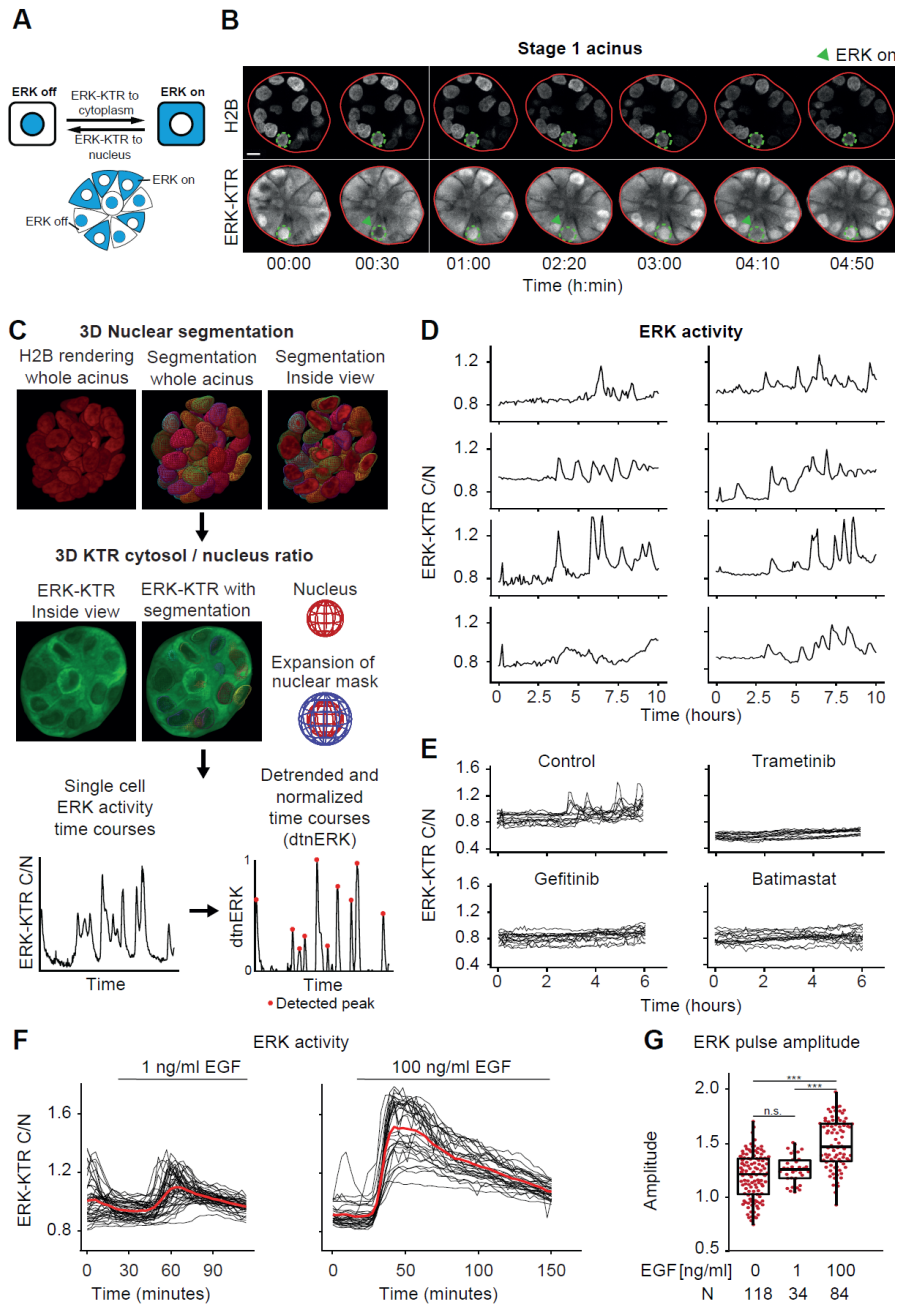
Figure 1 **Spontaneous EGFR/MMP-dependent ERK pulses in acini.** (A) Schematic representation of the ERK activity - dependent subcellular localization of ERK-KTR. (B) Time-series of the equatorial optical section of an acinus (red plain line) expressing fluorescent H2B and ERK-KTR. Highlighted is a cell (green dotted line) that displays spontaneous ERK activity pulses (arrowheads) resulting in the nuclear to cytoplasmic translocation of ERK-KTR. Scale bar = 10 µm. (C) Image analysis pipeline to extract ERK trajectories from 3D time lapse datasets. Nuclei are segmented and tracked by LEVERJS based on the H2B signal. Single-cell ERK activity levels are the ratio of the median ERK-KTR signal pixel intensities in the voxel mask around the nucleus and the one of the segmented nuclear volume. ERK pulses are detected on detrended ERK trajectories normalized to [0,1]. (D) Representative single-cell ERK trajectories from one acinus. (E) Overlayed ERK trajectories from control and drug-treated acini. Control trajectories correspond to the same acinus as in (D). (F) ERK trajectories from acini treated with 1 or 100 ng/ml EGF at the indicated time points. (G) ERK pulse amplitudes in cells from control and EGF-treated acini. Wilcoxon tests (n.s., P > 0.05; ***, P < 0.001).

7
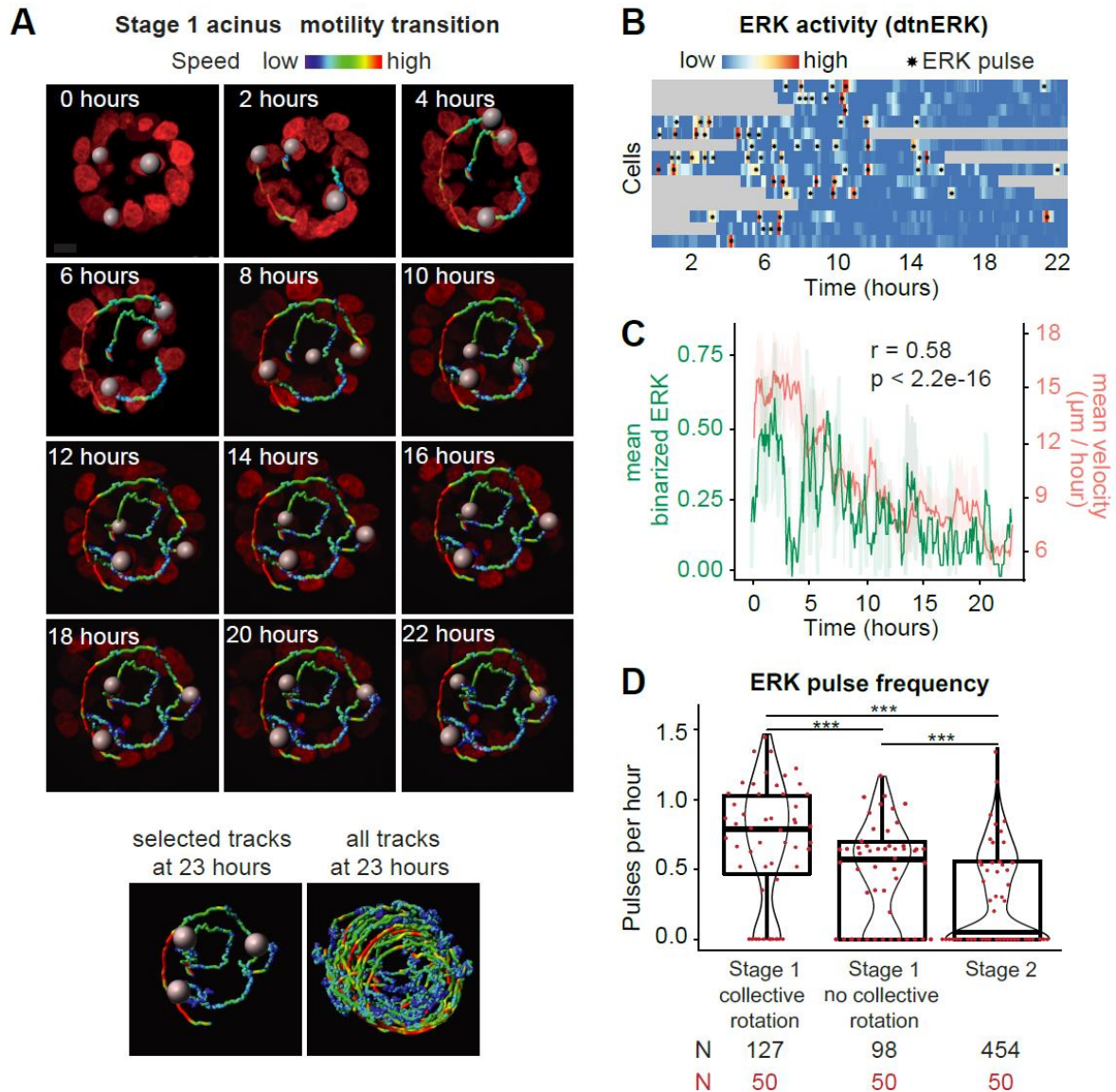
Figure 2 **Collective cell migration and ERK pulsing in stage 1 acini** (A) Time series renderings of the cross section of an acinus transitioning from the rapid motility to the slow motility stage. Nuclei and motility tracks color-coded by instantaneous velocity are shown. Scale bar = 10 µm. (B) Analysis of ERK activity in the acinus from (A). Heatmap shows detrended and normalized single cell ERK activity levels over time. Gray areas correspond to time points when a cell was not within the imaged volume. Asterisks indicate individual ERK pulses. (C) Analysis of motility and ERK activity in the acinus from (A). Graph shows mean binarized ERK activity and mean instantaneous velocity with 95% confidence intervals of all imaged cells over time and their Pearson correlation coefficient. Mean binarized ERK activity is used as a measure for the fraction of the cell population in a state of active ERK. (D) ERK pulse frequency from trajectories at different developmental timepoints. Trajectories pooled from 7 (stage 1 rotation), 5 (stage 1 no rotation) and 11 (stage 2) acini. Wilcoxon tests (***, P < 0.001).

Stage 2 quiescent acini exhibit different ERK frequencies in inner and outer cells, which emerges from collective waves of ERK pulses.

We then evaluated ERK dynamics in larger, stage 2 quiescent acini that are characterized by an outer layer of polarized cells, and a less organized inner cell mass destined for apoptosis for future lumen formation (Debnath et al., 2002). When comparing low-motility stage 1 and stage 2 acini, we observed a further reduction in median ERK frequency (Figure 2D), while ERK pulse amplitudes and durations remained almost identical (Figure S3B,C). This change in ERK frequency resulted from a bimodal distribution in which a part of the cell population did not display any ERK pulses (Figure 2D). Because ERK pulse frequency can regulate proliferation, survival and apoptosis fates in MCF10A cells (Aikin et al., 2020; Albeck et al., 2013; Gagliardi et al., 2021), and because inner cells in stage 2 acini are destined to undergo apoptosis, we evaluated ERK pulse frequencies in inner versus outer cells. Outer cells exhibited a significantly higher ERK frequency than inner cells, with the latter often not exhibiting ERK pulses at all (Figure 3A,B). Similar ERK activity amplitude and duration were found in inner/outer cells (Figure S3D,E). Together with our characterization of fate decisions (Figure S1), these results suggest a spatio-temporal mechanism that controls survival versus apoptosis fates through regulation of ERK frequency.

A striking feature of stage 2 acini was that they exhibited spatially correlated ERK pulses in the form of waves spreading across multiple cells (Figure 3B,C, Movie S3). We devised computational methods (Figure S3F-H, Materials and Methods) to detect, track, and extract features that describe ERK waves. These ERK waves were observed in all of the stage 2 acini that we imaged (N=11), and exhibited different geometries (Figure 3D). While some ERK pulses remained restricted to single cells, most of the ERK pulses occurred within collective waves (Figure 3E). ERK waves typically involved a median of 6 cells for a median duration of 54 minutes (Figure 3F,G). However, a large variance was observed with some ERK waves involving as little as 2 and as many as 39 cells (almost the whole acinus). ERK waves, as well as isolated ERK pulses, were predominantly initiated in the outer cell layer (Figure 3H). Further, ERK waves that originated in the outer layer displayed a higher bias to remain at that location than those originating in inner cells (Figure 3I). We have previously shown that in 2D MCF10A cultures, as well as in acini, apoptotic cells trigger ERK waves in their neighboring cells (Gagliardi et al., 2021). However, the ERK waves we

206 observed here only rarely coincided with apoptotic events, suggesting that they

207 originate through a different mechanism. Our results strongly suggest that ERK waves

208 contribute to spatially position different ERK pulse frequencies in inner and outer

209 acinar cells.
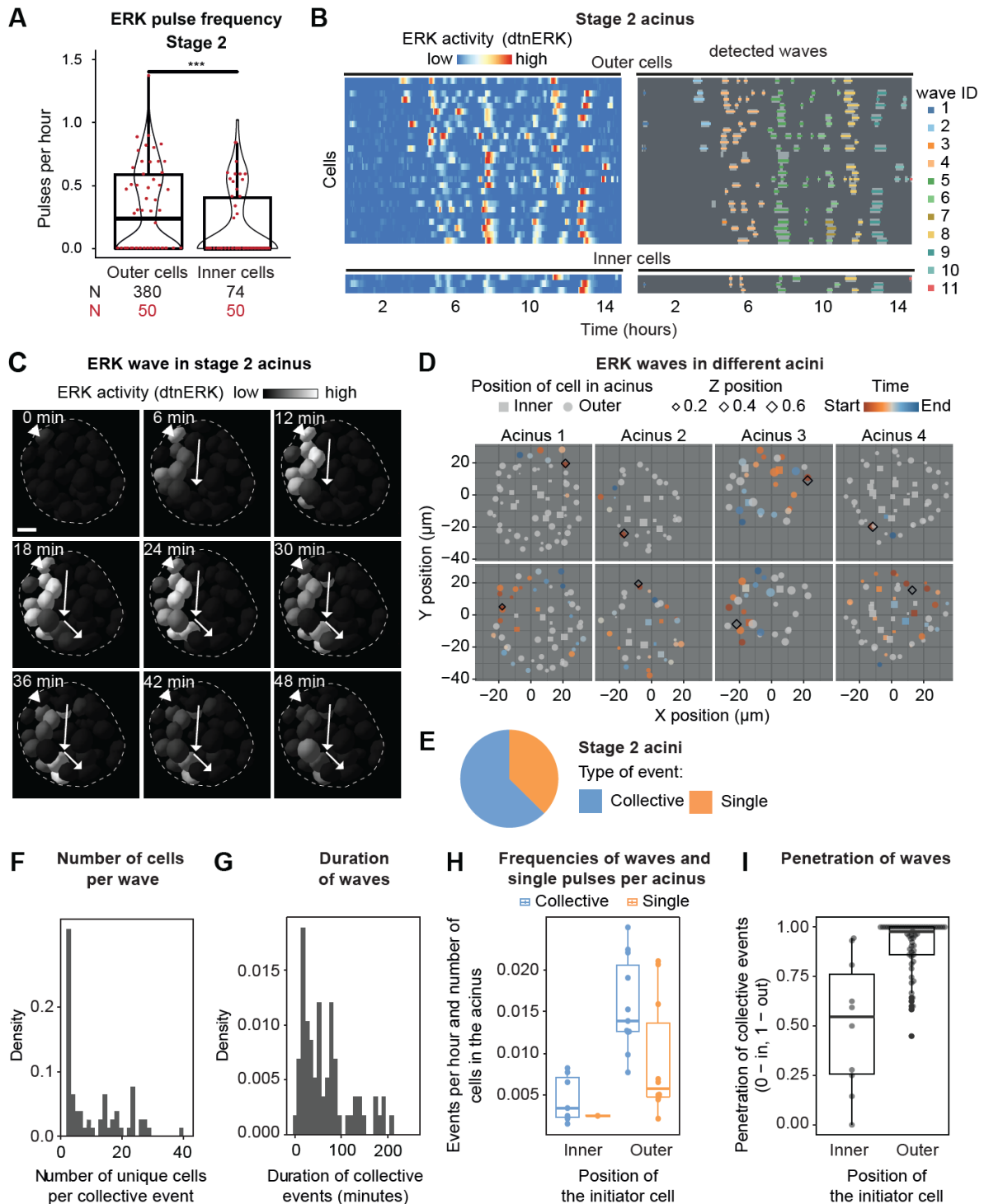
Figure 3 **Different ERK pulse frequencies in inner and outer acinar cell layers in stage 2, and collective waves of ERK pulses.** (A) ERK pulse frequency from trajectories of cells located in inner versus outer acini layers. Trajectories pooled from 11 acini. Wilcoxon test (***, P < 0.001). (B) Left: heatmap of detrended/normalized single-cell ERK trajectories in outer and inner cells of a representative acinus. Right: detection of individual ERK activity waves in the same acinus. (C) Representative time-series micrographs of ERK wave ID 10 in (B). Nuclei color-coded by ERK-KTR ratios. Arrows depict wave directionality. The arrowhead indicates the initiator cell. Dashed line indicates the acinus border. Scale bar = 10 μm. (D) 2D projection representations of isolated ERK waves from four different acini. Cells that participate in the wave are color-coded by their relative time of activation. Size represents the relative Z position of the cell and shape if they belong to the inner or outer cell population. Top and bottom panels

221   depict two isolated ERK waves for each acinus. (E) Percentage of initiator events that remain
222   restricted to a single cell vs those that lead to collective events. (F) Total numbers of unique
223   cells involved in individual collective events. (G) Durations of individual collective events. (H)
224   Average frequency of single and collective events per acinus, normalized by the number of
225   cells in the acinus. (I) Penetration of collective events across acini. Calculated as the time-
226   averaged fraction of localization of a collective event between the inner (0) and outer (1) cell
227   layer.

Optogenetic control of ERK frequency regulates collective motility, survival and apoptosis fates

228
229

230   To explore the role of ERK pulse frequency during stage 1 collective motility, as well
231   as stage 2 apoptosis and survival fates required for lumen morphogenesis, we used
232   two optogenetic actuators to evoke different ERK pulse frequencies in acini (Figure
233   4A). Optogenetic fibroblast growth factor receptor (optoFGFR) is a Cry2-based light-
234   activatable receptor tyrosine kinase that activates ERK, Akt and calcium signaling (Kim
235   et al., 2014). OptoRaf is a CIBN/Cry2-based system in which a catalytic Raf domain is
236   recruited to a plasma membrane targeted anchor in a light-dependent fashion to
237   specifically activate ERK (Aoki et al., 2017). We generated stable lines expressing any
238   of the two optogenetic constructs, a spectrally compatible ERK-KTR-mRuby, and H2B-
239   miRFP. Application of a single blue light pulse evoked a discrete optoFGFR- or
240   optoRaf-mediated ERK pulse with similar shape and duration as spontaneous ones
241   (Figure 4B).

242   Since ERK pulse wave patterns can coordinate collective cell migration through
243   regulation of myosin activity (Aoki et al., 2017; Hino et al., 2020), we hypothesized that
244   the asynchronous ERK pulses we observed might coordinate the collective motility
245   pattern in stage 1 acini. We therefore sought to disrupt this process by synchronizing
246   ERK pulses across all the cells of an acinus. We imaged rotating stage 1 acini for 4
247   hours in the absence of blue light, and observed asynchronous ERK pulses (Figure
248   4C). We then applied high frequency light pulses at 30 minute intervals, which
249   synchronized ERK pulses across cells (Figure 4C, Movie S4). This switch to
250   synchronous high-frequency ERK pulsing in all cells immediately resulted in
251   decreased cell migration speed and persistence (Figure 4D-F). This suggest that the
252   asynchronous high frequency ERK pulses organize collective cell migration in stage 1
253   acini.

254   Next, we tested the hypothesis that the different ERK frequencies observed between
255   outer and inner cells in stage 2 acini regulate survival vs apoptosis cell fates. Using
256   optoFGFR and optoRaf, we evoked frequency-modulated, population-synchronous
257   ERK dynamics in all the cells of an acinus (Figure 5A, Movie S5). Endogenous
258   collective ERK pulses were however still occurring. Because the regulation of
259   apoptosis/survival fates required for lumen formation spans over one week, we could
260   not use our live cell imaging platform to study this process. We therefore used LITOS
261   (LED Illumination Tool for Optogenetic Stimulation) (Höhener et al., 2022) to evoke

262   frequency-modulated ERK pulse regimes in multiwell plates in a tissue culture

263   incubator (Figure S4A). This system evoked similar ERK pulses as observed in our

264   live cell imaging system (Figure S4B). We then stimulated stage 2 acini with light

265   pulses delivered at different frequencies for 7 days and scored the distribution of acini

266   that exhibited filled lumen, partially cleared lumen or cleared lumen (Figure 5B). Using

267   both optoFGFR and optoRaf, we observed that ERK pulses induced every 0.5, 1, 2,

268   3, 4 but not 10 hours led to survival of inner cells, increasing the number of acini with

269   filled or partially cleared lumina (Figure 5C). These results further suggest that survival

270   and apoptosis fates are regulated by a frequency encoded ERK signal. The optoRaf

271   experiments indicate that high frequency ERK pulsing alone is sufficient to induce

272   survival independently of PI3K/Akt signaling.

273   Because endogenous ERK pulses occur on top of optogenetically-induced ones, we

274   used optoFGFR to evoke different ERK pulse frequencies in EGFR-inhibited acini that

275   do not exhibit spontaneous ERK pulses. Here, unstimulated acini and those stimulated

276   every 10 hours displayed cell death. In marked contrast, ERK pulses applied at 0.5, 1,

277   2, 3 or 4 hours led to cell survival (Figure 5D). These results show that cells in acini

278   must experience at least one ERK pulse every 4 hours to survive.

14
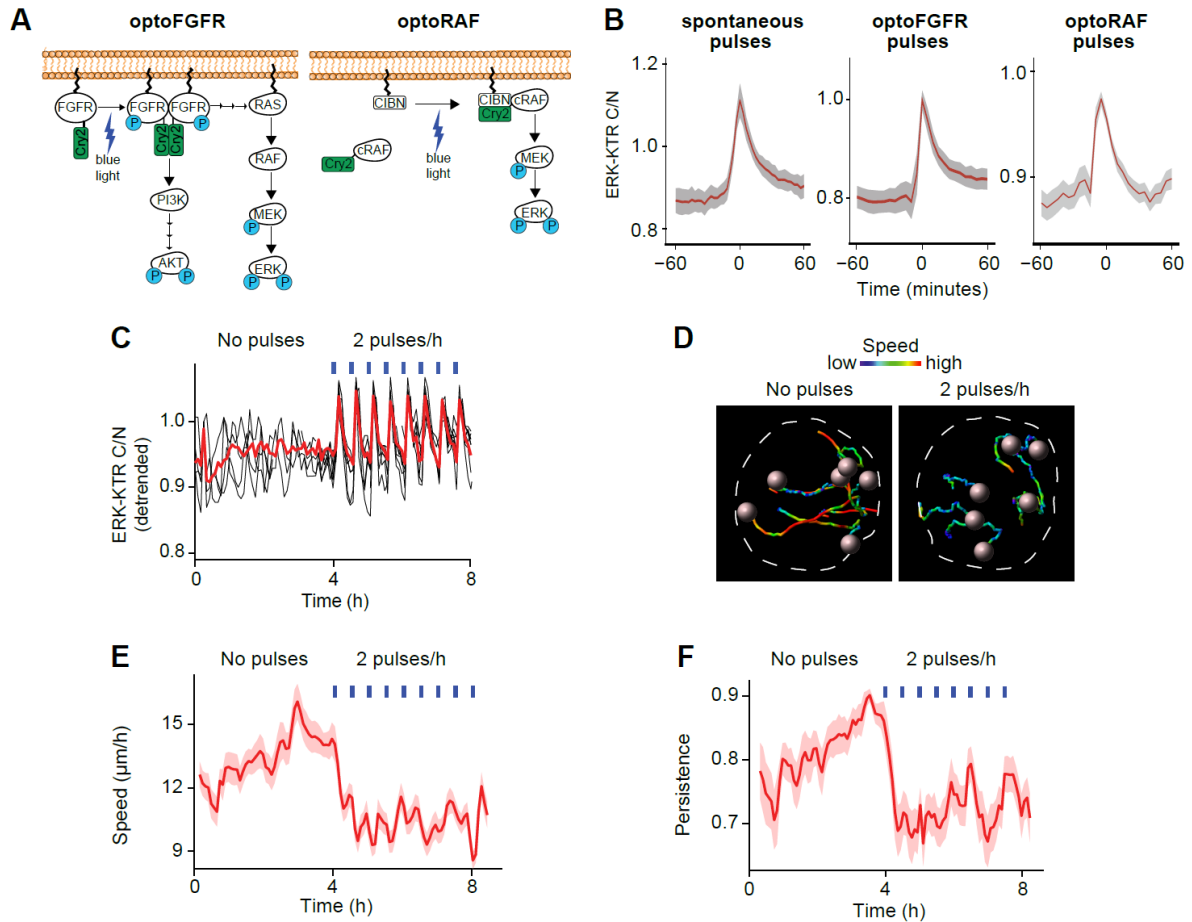
Figure 4 **Optogenetic stimulation of acini controls 3D migration properties in stage 1 acini** (A) Cartoon of the optoFGFR and optoRAF systems. OptoFGFR consists of the intracellular domain of FGFR1 linked to the plasma membrane and a Cry2 PHR domain which dimerizes upon blue light stimulation, leading to receptor autophosphorylation and activation of downstream cascades. OptoRAF consists of a Cry2 linked to cRaf and a membrane-linked CIBN domain. CIBN and Cry2 dimerize upon blue light stimulation which recruits cRaf to the plasma membrane where it phosphorylates MEK. (B) Average ERK trajectories from isolated spontaneous and optogenetically induced ERK pulses with 95% confidence interval. Time = 0 corresponds to maximal amplitude of peaks. (C) Overlayed detrended ERK activity trajectories from a stage 1 rotating acinus expressing optoFGFR and stimulated every 30 min starting from 4 hours. Vertical blue lines indicate the blue light stimulation. (D) Six single-cell migration trajectories from the same example organoid color coded according to migration speed. Spheres represent the nuclei positions at the end of the trajectory. The micrographs were taken at 4 and 8 hours of the experiment, each one with the migration trajectories of the past 4 hours. Dashed line indicates the acinar border. (E) Speed and (F) persistence of single-cell migration in the same acinus. Population average and 90% confidence interval are shown.
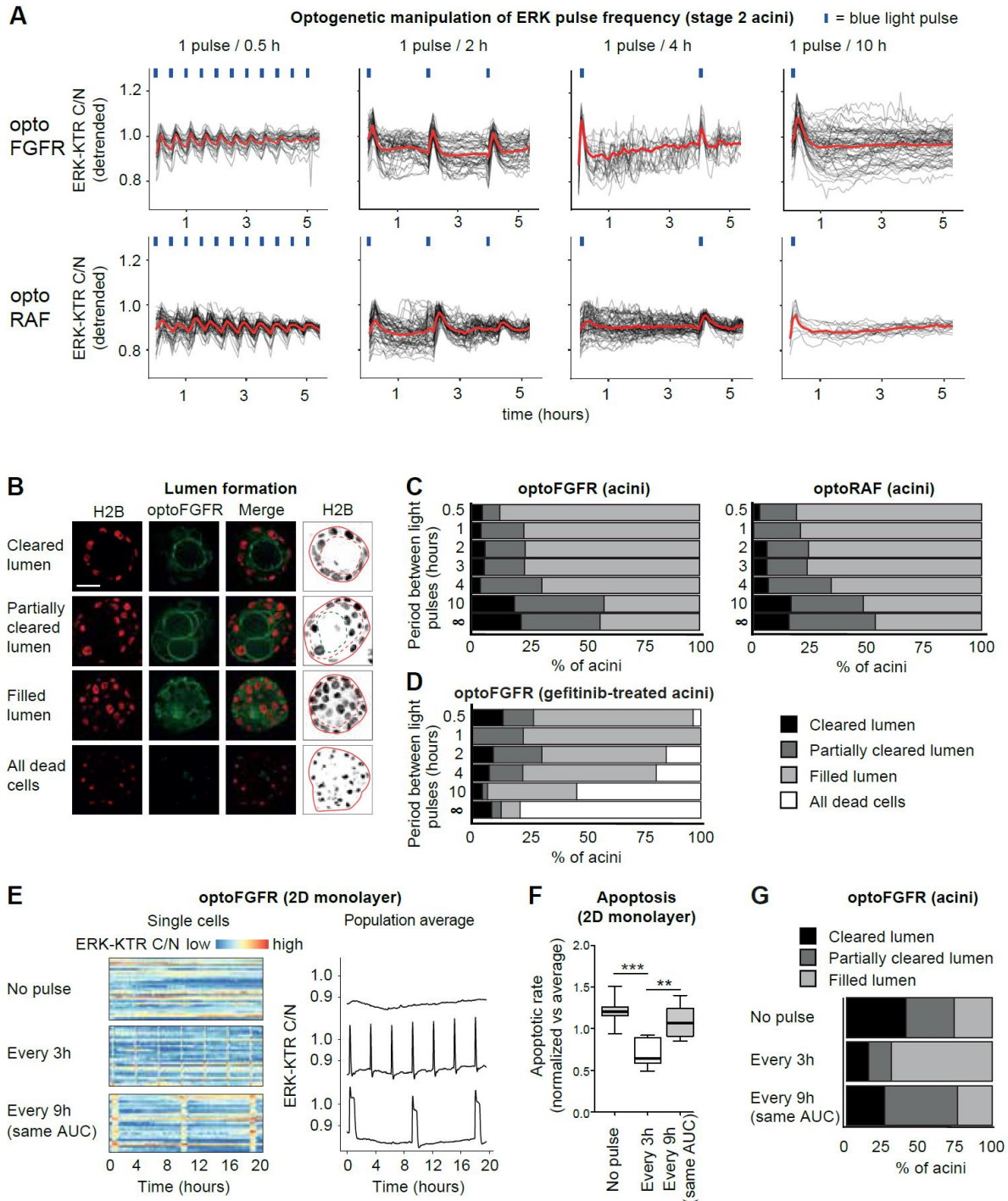
15

Figure 5 **Controlling survival/apoptosis decisions with optogenetic actuators.** (A) Overlayed detrended ERK activity trajectories from optoFGFR or optoRAF expressing acinar cells stimulated with different blue light pulse frequencies. (B) Colored: Equatorial optical sections of acini displaying cleared, partially cleared or filled luminal space or underwent complete cell death at stage 4. Black and white: maximal intensity projections of equatorial Z planes spanning 12 μm. Acini borders (red lines), luminal space (dashed red lines), and the border between the cleared and filled part of the luminal space (dashed green lines) are indicated. Scale bar = 20 μm. (C) Percentages of acini displaying cleared, partially cleared or filled luminal space at day 14, after 7 days on an LED plate that emitted blue light pulses at defined intervals. N = 36 - 72 acini per condition from 2 independent replicates. Pearson's chi-squared test. optoFGFR: X^2 (12 degrees of freedom, N = 384) = 78, P < 0.001. optoRAF: X^2 (12 degrees of freedom, N = 326) = 32, P < 0.005 (D) Percentages of acini displaying cleared,

16

307   partially cleared or filled luminal space or complete cell death at day 14, after 7 days in the
308   presence of gefitinib on an LED plate that emitted blue light pulses at defined intervals. N =
309   24 - 46 acini per condition. X^2 (15 degrees of freedom, N = 201) = 79, P < 0.001. (E) MCF10A
310   cells in monolayer culture were stimulated every 3 hours with blue light pulses or every 9 hours
311   with the same AUC, achieved with 20 consecutive blue light pulses, and compared with
312   unstimulated cells. Randomly selected trajectories (left) and whole population average (right).
313   (F) Distribution of apoptotic rates in 5 biological replicates each one normalized on the
314   experiment mean. t-test (**, P < 0.01; ***, P < 0.001). (G) Percentages of optoFGFR-
315   expressing acini that displayed cleared, partially cleared or filled luminal space at day 14, after
316   7 days on an LED plate that emitted either a single blue light pulse every 3 hours, 20
317   subsequent blue light pulses every 9 hours or no blue light pulses. N = 27-39 acini per
318   condition. X^2 (4 degrees of freedom, N = 104) = 23, P < .001.

319   **ERK frequency but not integrated ERK activity regulates the survival fate** Next,

320   we explored if the frequency of ERK pulses or the total integrated ERK activity over

321   time controls survival. To test this, we used optoFGFR to induce synthetic ERK

322   pulses of different widths, that when applied at different frequencies can evoke the

323   same integrated ERK activity over a specific time period. Since ERK pulses display an

324   identical shape and promote survival for 4 hours both in serum-deprived 2D

325   monolayers (Gagliardi et al., 2021) and 3D acini, we first identified light stimulation

326   schemes capable of inducing ERK pulses of different widths in monolayers. We

327   applied a series of 1 to 86 successive blue light pulses delivered at 2-minute intervals,

328   and recorded the resulting ERK dynamics (Figure S4C). We have previously shown

329   that light stimulation applied at this frequency leads to sustained optoFGFR activity

330   (Dessauges et al., 2021). The integrated ERK activity (area under the curve = AUC)

331   displayed a linear relationship with the number of light pulses (Figure S4D). 20 blue

332   light pulses delivered every 2 minutes led to a single ERK pulse with a three-fold

333   increase in integrated ERK activity. We then applied 2 distinct optoFGFR stimulation

334   schemes consisting of 1 AUC equivalent of ERK activity evoked every 3 hours versus

335   3 AUC equivalents of ERK activity evoked every 9 hours, resulting in the identical

336   integrated ERK activity over a period of 9 hours (Figure 5E). We found that the first

337   but not second optogenetic stimulation scheme induced cell survival in serum-

338   deprived 2D cultures (Figure 5F). We then performed the identical experiment in stage

339   2 acini by applying the two optogenetic stimulation schemes using LITOS for 7 days.

340   Quantification of lumen formation efficiency at day 14 revealed increased inner cell

341   survival when the first, but not the second, optogenetic stimulation scheme was

342   applied (Figure 5G). These results show that the frequency of ERK pulses rather than

343   the integrated ERK activity regulates survival.

344   Finally, we also used our optogenetic toolkit to explore a number of scenarios of how

345   different ERK frequencies in inner/outer cells might be regulated in stage 2 acini.

346   These results are discussed in the Supplemental Text and Figure S5.

347

348   **Oncogenic PI3K signaling increases ERK frequency leading to loss of acinar**

349   **lumen formation**

350   We then explored ERK dynamics in the context of a pathological alteration of acinar

351   morphogenesis induced by the H1047R mutation in the alpha subunit of PI3K

352   (PIK3CA), which is frequently mutated in breast cancer (Cancer Genome Atlas

18

353   Network, 2012). The H1047R PIK3CA mutation leads to absence of lumen in MCF10A

354   knockin acini (Berglund et al., 2013; Chakrabarty et al., 2010; Chen et al., 2013, Isakoff

355   et al., 2005; Lauring et al., 2010), as well as ductal hyperplasia in a transgenic mouse

356   model (Tikoo et al., 2012). H1047R PIK3CA MCF10A knock-in cells have been shown

357   to display elevated ERK activity using western blot (Gustin et al., 2009), strongly

358   suggesting the existence of a crosstalk between oncogenic PI3K and MAPK/ERK

359   signaling. Consistently, we found that H1047R PIK3CA MCF10A knock-in cells

360   cultured as monolayers displayed higher median ERK frequency than their wild-type

361   (WT) counterparts (Figure 6A-C), while maintaining similar ERK pulse shape, duration

362   and amplitude (Figure 6D, S6A,B). The finding of a similar ERK pulse shape in WT

363   and mutant cells indicates that the PI3K to MAPK crosstalk must occur upstream of

364   Ras because the MAPK network structure that shapes ERK dynamics is maintained

365   (Kholodenko et al., 2010). The increased ERK frequency suggests the involvement of

366   receptor   level   interactions   (Sparta   et   al.,   2015).

367   To better understand the effect of the PIK3CA H1047R on acinar morphogenesis, we

368   evaluated proliferation and apoptosis during different stages (Figure 6E-I). Stage 1

369   mutant acini displayed increased proliferation compared to their WT counterparts, as

370   evidenced by augmented cell numbers, and geminin quantification (Figure 6E-G).

371   While remaining slightly higher than in WT acini, proliferation also diminished during

372   stages 2 - 4, but displayed a small upshoot during stage 4 (Figure 6E,G). In contrast

373   to the steep apoptosis rise observed starting on day 7 in WT acini, apoptotic rates

374   remained lower in PIK3CA mutant acini at all stages (Figure 6E,H). Increased

375   proliferation at stage 1, and decreased apoptosis at stages 3 and 4, thus mostly

376   contribute to increased cell number and absence of lumen formation in PIK3CA-

377   mutant acini (Figure 6I).

378   We then evaluated ERK dynamics during the pathological acinar morphogenesis

379   induced by PIK3CA H1047R. As in monolayers, PIK3CA-mutant acini displayed ERK

380   pulses like those of WT acini (Figure 7A). Stage 1 rotating PIK3CA-mutant acini

381   displayed ERK frequencies as high as those observed in their WT counterparts (Figure

382   7B). However, stage 1 non-rotating PIK3CA-mutant acini did not display the decreased

383   ERK frequency observed in WT (Figure 7B). Stage 2 PIK3CA-mutant acini displayed

384   increased ERK frequency compared to WT, as well as prominent ERK waves (Figure

385   7B-D, Movie S6). However, most likely due to their heterogeneity, we could not

386   pinpoint a specific feature of ERK waves associated with the increased ERK frequency

387   observed in PIK3CA-mutant versus WT acini. PIK3CA-mutant stage 2 displayed

388   higher ERK frequencies than WT acini, leading the inner cells of PIK3CA-mutant to

389   exhibit a similar ERK frequency than the outer cells of WT acini (Figure 7B,C).

390   Amplitude and duration of ERK pulses were similar for both WT and PIK3CA H1047R

391   acinar cells at all stages (Figure S6C,D).

392   Pictilisib-mediated PI3K or AZD5363-mediated Akt inhibition decreased ERK

393   frequency in both WT and mutant acini (Figure 7E). Stimulation of WT acini with

394   insulin-like growth factor (IGF1), that primarily activates PI3K-Akt signaling (Myers et

395   al., 1993), also resulted in increased ERK pulse frequency (Figure S7A,B). Gefitinib-

396   mediated EGFR inhibition abolished ERK pulses in PIK3CA-mutant acini, suggesting

397   an EGFR-dependent mechanism (Figure S7C). Batimastat-mediated MMP inhibition

398   in PIK3CA H1047R cells led to reduction of ERK phosphorylation to levels

399   observed in WT cells, without affecting Akt signaling (Figure S7D). PIK3CA

400   H1047R MCF10A cells have been shown to exhibit increased expression of

401   the EGFR-ligand amphiregulin in comparison to WT cells (Young et al., 2015),

402   possibly explaining the increase in EGFR-dependent ERK frequency. Consistently,

403   we observed increased amphiregulin expression at mRNA level in PI3K-mutant when

404   compared with WT cells. Amphiregulin expression levels were were decreased

405   upon pictilisib-mediated inhibition of PI3K activity in PIK3CA mutant cells (Figure

406   S7E). Together, these results strongly suggest that the PI3K to MAPK/ERK crosstalk

407   that regulates ERK frequency involves amphiregulin/MMP-activation of EGFR.

408   Increased survival in PIK3CA H1047R acini might therefore involve increased

409   ERK frequency through this crosstalk mechanism, in addition to PI3K-Akt signaling.
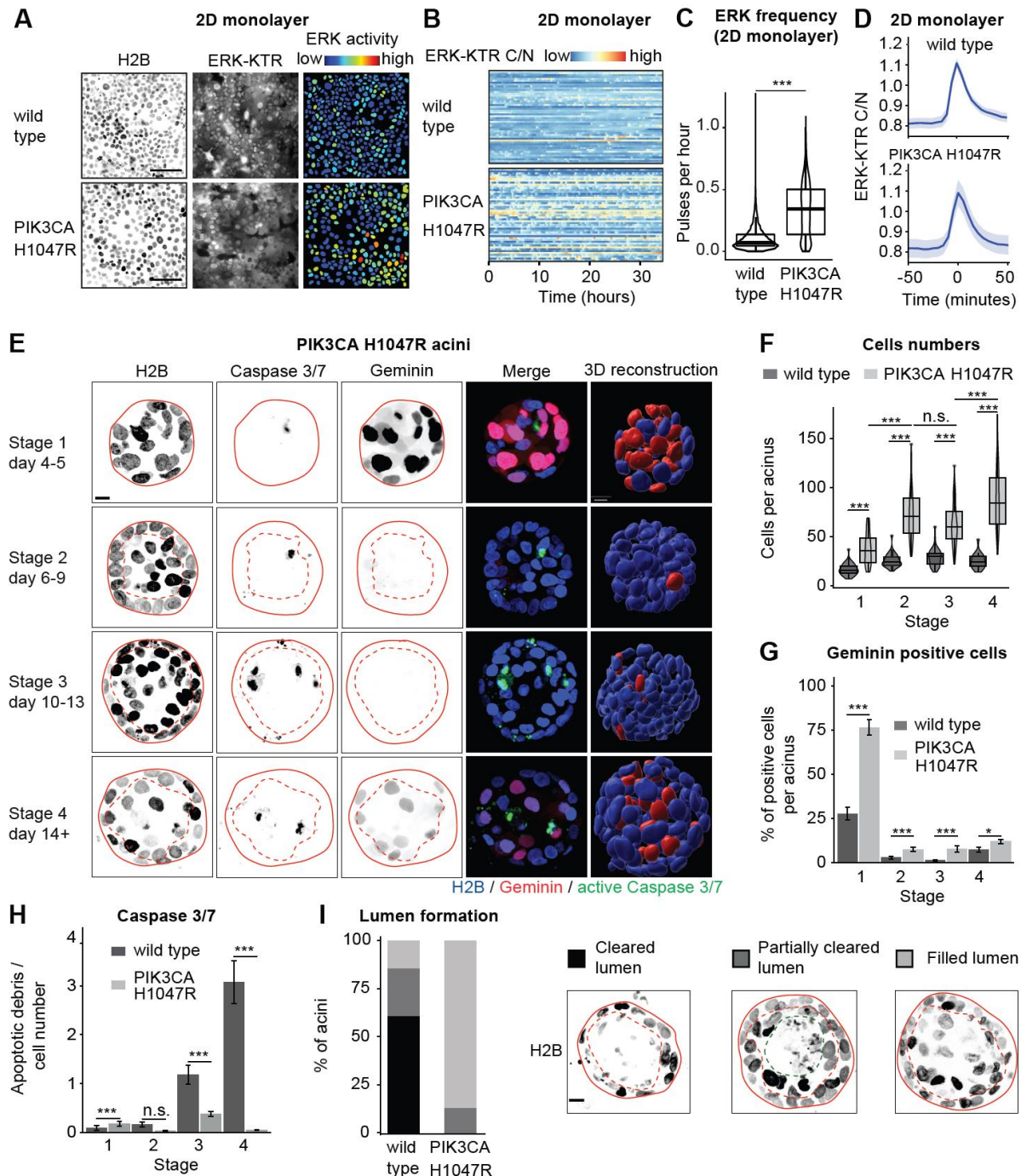
Figure 6 **Increased 2D monolayer ERK frequency and altered acinar morphogenesis of PIK3CA H1047R cells.** (A) Micrographs of WT and PIK3CA H1047R MCF10A 2D monolayers expressing fluorescent H2B (left) and ERK-KTR (middle). Right: nuclei of the same cells color-coded by ERK-KTR ratio. Scale bar = 100 µm. (B) Heatmap of single-cell ERK trajectories in WT and PIK3CA H1047R monolayers. (C) ERK frequencies in WT and PIK3CA H1047R monolayer cells. (D) Average ERK trajectories from isolated pulses in WT and PIK3CA H1047R cells within monolayers. 95% confidence intervals are shown. Time = 0 corresponds to maximal amplitude of peaks. (E) Micrographs and 3D reconstructions of H2B, caspase 3/7 fluorogenic substrate and geminin signals in PIK3CA H1047R acini at different stages. Micrographs show maximal intensity projections of equatorial Z planes spanning 12 µm. Plain lines mark the borders of the acini, dashed lines mark the outer cell layer. Scale bar = 10 µm. (F) Cell numbers per acinus at the different stages. N = 54 - 60 PIK3CA H1047R acini each. (G) Fraction of Geminin positive cells per acinus at different stages. (H) Number of Caspase

423   3/7 apoptotic debris divided by the acinar cell number at different days. (I) Percentages of
424   acini that either displayed a cleared, partially cleared or filled luminal space at day 14.
425   Pearson's chi-squared test: X^2 (2 degrees of freedom, N = 82) = 50, P < 0.001. Representative
426   examples used for classification are shown (maximal intensity projections of equatorial Z
427   planes spanning 12 μm). Acini borders (red lines), luminal space (dashed red lines), and the
428   border between the cleared and filled part of the luminal space (dashed green lines) are
429   indicated. Scale bar = 10 μm. (F-I) Measurements taken on the same acini. WT acini are the
430   same as in figure S1, for comparison. (G, H) Error bars represent standard error of the mean.
431   (C, F, G and H) Wilcoxon tests (n.s., P > 0.05; *, P < 0.05; **, P < 0.01; ***, P < 0.001).
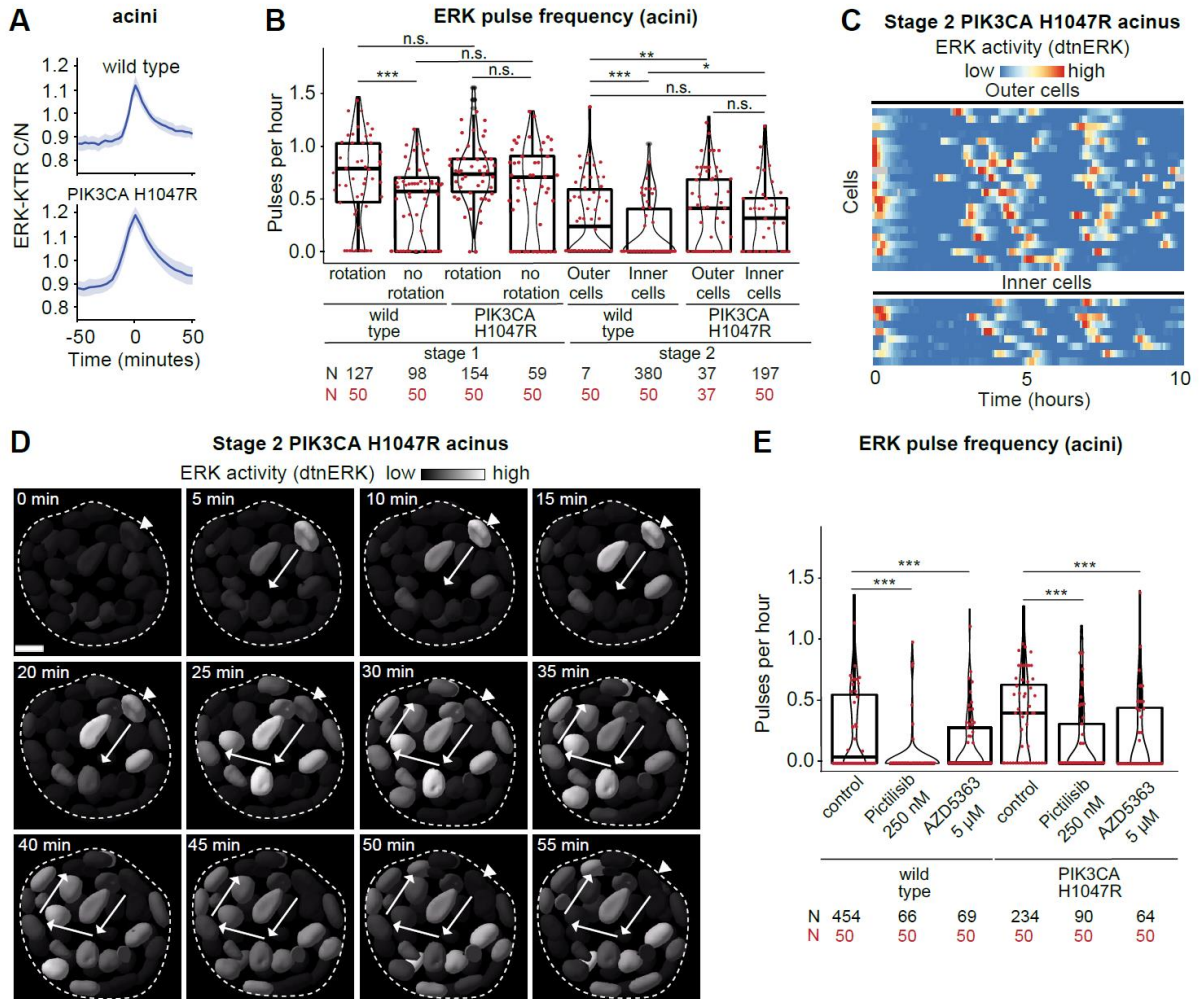
Figure 7 **Increased ERK frequency in PIK3CA H1047R mutant acini.** (A) Average ERK trajectories from isolated pulses in WT and PIK3CA H1047R cells within acini. 95% confidence intervals are shown. Time = 0 corresponds to maximal amplitude of peaks. (B) ERK frequencies of WT and PIK3CA H1047R cells at different stages and locations within the acinus. Mutant trajectories pooled from 7 (stage 1 rotation), 2 (stage 1 no rotation) and 6 (stage 2) acini. (C) Heatmap of detrended/normalized single-cell ERK trajectories in outer and inner cells of a representative stage 2 PIK3CA H1047R acinus. (D) Representative time-series of an ERK wave in a stage 2 PIK3CA H1047R acinus (dashed line) cross section. Nuclei are color-coded by ERK activity levels. Arrows show directionality of activation. Arrowhead indicates the initiator cell. Scale bar = 10 μm. (E) ERK frequencies of WT and PIK3CA H1047R cells from control acini and acini treated with 250 nM pictilisib or 5 μM AZD5363. (B and E) wt control data is the same as in figure 2 and 3, and shown again for comparison. Wilcoxon tests (n.s., $P > 0.05$; *, $P < 0.05$, **, $P < 0.01$; ***, $P < 0.001$).

23

Discussion

445   **Discussion**

446   Recent work in epithelial monolayers have revealed the existence of non-periodic

447   single-cell ERK pulses, whose frequency controls apoptosis, survival or proliferation

448   fates (Albeck et al., 2013; Aoki et al., 2013, Gagliardi et al., 2021; Valon et al., 2021).

449   At the level of a cell population, these ERK pulses can be stochastic when cells are

450   stimulated with EGF (Albeck et al., 2013), or can be organized as collective ERK

451   waves during collective cell migration (Aoki et al., 2017; Hino et al., 2020), cancer cell

452   extrusion (Aikin et al., 2020), or spatial regulation of survival in response to stress

453   (Gagliardi et al., 2021; Valon et al., 2021). Here we show that similar ERK

454   pulses/waves coordinate fate decisions during mammary acinar morphogenesis. As

455   in the cell systems mentioned above, ERK pulses are triggered by MMP-mediated

456   cleavage of pro-EGF ligands and subsequent activation of EGFR. Downstream of

457   EGFR, MAPK network properties such as ultrasensitivity and negative feedback

458   (Huang and Ferrell, 1996, Kholodenko et al., 2010) might allow to translate minute

459   amounts of MMP-cleaved pro-EGF into clear cut digital ERK pulses. Consistently, the

460   slightly lower amplitude of spontaneous ERK pulses versus those induced by acute

461   EGF stimulation suggests that the EGFR/MAPK system functions at the threshold

462   input to generate digital ERK pulses (Figure 1G). This might allow the

463   MMP/EGFR/MAPK signaling network to translate small variations in the EGFR input

464   into frequency-modulated regimes of ERK pulses that can specify proliferation,

465   survival and apoptosis. Note that exogenous addition of EGF impedes apoptosis-

466   mediated lumen formation (Gaiko-Shcherbak et al., 2015), further suggesting that

467   small amounts of EGFR ligands synthesized by the acinus itself are necessary for self-

468   organisation of its morphogenesis. This MMP/EGFR/MAPK network has also been

469   shown to produce ERK trigger waves in which activated cells sequentially switch on

470   ERK pulses in adjacent cells (Aoki et al., 2017; Boocock et al., 2020; Hino et al., 2020).

471   Our results strongly suggest that the ERK waves observed in stage 2 acini rely on this

472   mechanism. Thus, a relatively simple signaling network might allow to produce

473   conserved and sophisticated ERK behaviors in epithelial collectives. This excitable

474   MMP/EGFR/MAPK network that generates pulsatile ERK activity strongly contrasts

475   with the oscillatory ERK behavior observed in the segmentation clock in vertebrate

476   embryos that is regulated on slower timescales by rhythmic transcriptional regulation

477   of MAPK phosphatases (Hubaud and Pourquié, 2014). We speculate that the pulsatile

478   MAPK network observed in epithelia provides an opportunity to constantly sense and

479 react to environmental inputs such as growth factors and insults to warrant epithelial
480 homeostasis during acinar development. This illustrates how the MAPK network can
481 be differently wired to produce distinct ERK dynamics at different timescales
482 depending on the developmental context.

483

484 **ERK dynamics regulate collective migration and proliferation in stage 1 acini**
485 We found that stage 1 acini displayed high frequency, asynchronous ERK pulses
486 during rapid collective cell migration that leads to a global rotation behavior of the
487 acinus (Figure 2). This rotation behavior has previously been implicated in the
488 morphogenesis of spherical tissue buds during mammary organogenesis (Fernández
489 et al., 2021). During migration of 2D epithelial sheets, ERK waves co-ordinate myosin
490 activity necessary for collective motility, and are shaped by a mechanochemical
491 feedback from myosin to ERK (Aoki et al., 2017; Boocock et al., 2020; Hino et al.,
492 2020). Further, ERK also has been shown to control myosin activity in MCF10A acini
493 single-cell motility (Pearson and Hunter, 2007). We therefore propose that
494 asynchronous ERK pulses spatially coordinate myosin contractility necessary for this
495 collective motility behavior. This is consistent with our result that optogenetic
496 synchronization of ERK pulses immediately leads to decreased collective motility
497 (Figure 4C-F). The transition to a state of slower motility in late stage 1 acini has been
498 shown to result from assembly of an endogenous laminin-rich basement membrane
499 (Wang et al., 2013). We speculate that assembly of this basement membrane might
500 modify the myosin-ERK mechanochemical feedback loop mentioned above, leading
501 to decreased ERK frequency and motility, allowing to regulate the transition from
502 proliferation to quiescence. Assembly of the basement membrane might therefore act
503 as a checkpoint coordinating ERK frequency-dependent regulation of motility and
504 transition from proliferation to quiescence. Future experimental/modeling studies will
505 be necessary to further refine this hypothesis.

506

507 **ERK waves spatially regulate apoptosis and survival fates during stage 2 acinar**
508 **lumen morphogenesis**
509 Our experiments in stage 2 acini suggest that spatial control of different ERK
510 frequencies regulates survival in outer versus apoptosis fates in inner acinar cells.
511 Outer cells display a median ERK frequency of one pulse every 4 hours, while inner
512 cells display lower ERK frequencies (Figure 3A). This is consistent with the ability of

513   one ERK pulse to provide about 4 hours of survival in MCF10A monolayers (Gagliardi

514   et al., 2021). Using optogenetic control of ERK pulses, we excluded mechanisms such

515   as differential growth factor receptor sensitivity or refractory time of inner and outer

516   cells for regulation of different ERK frequencies (Supplementary Text, Figure S5A,B).

517   Instead, our results suggest a role for collective ERK waves to define the outer and

518   inner spatial domains of high and low ERK frequency, that respectively specify survival

519   and apoptosis fates (Figure 3B-I). ERK wave properties such as that they are initiated

520   mostly in the outer layer, and propagate more efficiently in the outer versus the inner

521   layer, might dynamically specify the two domains of ERK frequencies on timescale of

522   hours throughout the 7 days of the acinus cavitation process. While apoptosis is

523   predominantly responsible for the clearance of luminal cells in acini (Debnath et al.,

524   2002), we cannot exclude that an alternative mechanism such as autophagy resulting

525   from metabolic defects in inner cells, which is regulated by EGFR - PI3K signaling

526   might also contribute to this process (Schafer et al., 2009).

527

528   **ERK pulse frequency but not integrated activity regulates survival versus**

529   **apoptosis fates**

530   To formally test if ERK frequency regulates survival/apoptosis fates, we used

531   optogenetic stimulation of all the cells of acini to causally link ERK frequency with

532   lumen formation. When used to evoke ERK pulses for up to at least every 4 hours,

533   both optoFGFR and optoRaf led to loss of lumen formation (Figure 5C). ERK pulses

534   evoked every 10 hours were not sufficient to rescue apoptosis. These experiments

535   also functioned when EGFR was completely inhibited (Figure 5D). By optogenetically

536   varying the ERK pulse width, we also showed that ERK frequency rather than the

537   integrated ERK activity over time regulates survival versus apoptosis fates, both in

538   monolayers and in stage 2 acinus lumen formation (Figure 5E-G). Our data therefore

539   suggests that short ERK pulses are the signaling unit that allows cells in acini to

540   commit to survival for about 4 hours. This might allow cells to integrate signaling inputs

541   that fluctuate on timescales of minutes/hours, to dynamically control a morphogenetic

542   program on timescales of days. Interpretation of a specific ERK frequency into

543   survival/apoptosis fates might involve the ERK substrate Bcl-2-like protein 11 (Harada

544   et al., 2004) or ERK-dependent transcriptional control of immediate early genes (IEGs)

545   (Avraham and Yarden, 2011). IEGs produce transcripts with lifetimes of around 30

546   minutes, that encode proteins with lifetimes of 1-3 hours. Notably, IEGs include Jun

547 and Fos transcription factors which are important regulators of cell survival (Shaulian

548 and Karin, 2001). IEG's short lifetime is compatible with the ERK frequency required

549 for survival. Higher ERK frequencies as observed in stage 1 acini might control

550 proliferation by regulation of IEGs such as Fra-1 (Gillies et al., 2017).

551

552 **Oncogenic PI3K signaling modulates ERK frequency contributing to aberrant**

553 **acinar morphogenesis.**

554 Our results show that the breast cancer relevant PIK3CA H1047R mutation increases

555 ERK frequency, which might contribute at least in part to increased proliferation and

556 survival leading to larger acini without lumen formation, that phenocopies ductal

557 hyperplasia observed in mouse models (Tikoo et al., 2012). We show that this

558 crosstalk from PI3K to ERK signaling feeds into the control of ERK frequency both in

559 WT and PIK3CA H1047R monolayers and acini (Figure 7, S6-7). This crosstalk also

560 functions downstream of IGF1, that primarily activates PI3K-Akt signaling (Myers et

561 al., 1993) (Figure S7A,B), suggesting that it is a conserved feature downstream of

562 multiple receptor tyrosine kinases. During stage 1, PIK3CA H1047R acini display

563 similarly high ERK frequencies as in WT acini (Figure 7B). During stage 2, PIK3CA

564 H1047R acini then still display a substantial decrease in ERK frequency as in WT acini

565 compared to stage 1 (Figure 7B), which correlates with decreased proliferation (Figure

566 6E-H). However, ERK frequencies remain slightly higher both in outer and inner cells

567 in PIK3CA H1047R versus WT acini, correlating with the strong survival phenotype in

568 inner cells, and absence of lumen formation. These results suggest that the control of

569 ERK frequency is still subject to some degree of regulation even when the crosstalk

570 from PIK3CA H1047R is constitutively switched on. Because the ERK pulse shape is

571 identical in WT and PIK3CA mutant cells, this crosstalk must occur upstream of the

572 core Raf/MEK/ERK circuit. Consistently, ERK activation is sensitive to both EGFR and

573 MMP inhibition in PIK3CA H1047R cells (Figure S7C,D). As reported previously

574 (Young et al., 2015), our data strongly suggests that constitutive PI3K activity in

575 PIK3CA H1047R cells leads to increased expression of the EGFR ligand amphiregulin

576 that in turn might increase ERK frequency (Sternlicht et al., 2005) (Figure S7E).

577 PIK3CA H1047R also has been found to decrease expression of the protein tyrosine

578 phosphatase receptor type F (PTPRF) (Young et al., 2015), which might further

579 augment EGFR excitability and thus ERK frequency. Further work is required to

580 elucidate the specific contributions of PI3K and ERK signaling to control the

27

581 survival/apoptosis fate decisions and how the PI3K/ERK crosstalk might spatially fine

582 tune ERK frequency. Our result strongly suggests that oncogenic PI3K signaling-

583 induced aberrant spatial regulation of ERK frequency contributes to pathological

584 acinar morphogenesis.

585

586 **Conclusion**

587 We provide an initial characterization into how single-cell ERK dynamics control fate

588 decisions in space and time during the morphogenesis of a simple prototype organ

589 structure. Future studies are required to mechanistically understand how the different

590 dynamic signaling states are encoded and spatially organized, and if they provide

591 robustness against environmental perturbations occurring during development. This

592 will require the ever-expanding arsenal of optogenetic tools to manipulate specific cells

593 and evaluate how the cell collective responds. Further questions include how

594 additional signaling pathways might fine tune this morphogenetic process, and how

595 the ERK frequency is decoded into transcriptional programs that actuate the different

596 fates that shape acinus morphogenesis.

Material and methods

2D cell culture

MCF10A cells were cultured in DMEM/F12 supplemented with 5% horse serum, 20 ng/ml recombinant human EGF (Peprotech), 0.5 µg/ml hydrocortisone (Sigma-Aldrich/Merck), 10 µg/ml insulin (Sigma-Aldrich/Merck), 200 U/ml penicillin and 200 µg/ml streptomycin. The PIK3CA H1047R knockin cell line (Gustin et al., 2009) was a gift of Ben Ho Park. We regularly verified the presence of the mutation by sequencing the corresponding genomic locus. To generate stable cell lines, cells were transfected with FuGene (Promega) according to the manufacturer's protocol and clones were selected by antibiotic resistance and image-based screening.

3D cell culture

For acinus formation, single MCF10A cell suspensions were mixed with 4 volumes of growth factor-reduced Matrigel (Corning) at 4 °C and spread evenly on the surface of glass bottom cell culture plates at a concentration of 1.5×10^4 cells/cm^2. Acini were cultured in DMEM/F12 supplemented with 2% horse serum, 20 ng/ml recombinant human EGF, 0.5 µg/ml hydrocortisone, 10 µg/ml insulin, 200 U/ml penicillin and 200 µg/ml streptomycin. Horse serum, insulin and EGF were removed after 3 days of culture. For live imaging, 25 mM Hepes was added to the medium prior to mounting on the microscope. CellEvent Caspase 3/7 Green Detection Reagent was obtained from Thermo Fisher Scientific and used according to the manufacturer's protocol.

Plasmids

ERK-KTR-mTurquoise2 and ERK-KTR-mRuby2 were generated by fusion of the coding region of ERK-KTR (Regot et al., 2014) with that of mTurquoise2 (Goedhart et al., 2012) or mRuby2 (Lam et al., 2012). H2B-miRFP703 was generated by fusion of the coding region of human H2B clustered histone 11 (H2BC11) with that of miRFP703 (Shcherbakova et al., 2016). Geminin-mCherry was generated by fusion of the ubiquitylation domain of human Geminin (Sakaue-Sawano et al., 2017) to mCherry. The above mentioned fusion proteins were cloned in the piggyBac vectors pMP-PB, pSB-HPB (Balasubramanian et al., 2016) (gift of David Hacker, EPFL), or pPB3.0.Blast, an improved version of pPB generated in our lab.

pPB3.0-PuroCRY2-cRAF-mCitrine-P2A-CIBN-KrasCT, referred to in the manuscript

29

631   as OptoRAF, was generated in the following way: The CRY2-cRaf sequence was

632   excised from pCX4puro-CRY2-cRAF (gift from Kazuhiro Aoki, (Aoki et al., 2017))

633   using EcoRI and NotI. mCitrine was PCR amplified from the optoFGFR plasmid, while

634   adding NotI and XhoI sites, and digested. Both sequences were ligated into pPB3.0-

635   Puro, previously digested with EcoRI and XhoI. The GSGP2A-CIBN-KRasCT

636   sequence (synthesized by GENEWIZ) was digested with BsrGI and AflII and ligated

637   into pPB3.0-Puro-CRY2-cRAF-mCitrine.

638   The piggyBac plasmids were co-transfected with a helper plasmid expressing a

639   hyperactive piggyBac transposase (Yusa et al., 2011).

640   Lyn-cytoFGFR1-PHR-mCit, expressing myristoylated FGFR1 cytoplasmic region

641   fused with the PHR domain of cryptochrome2 and mCitrine (gift from Won Do Heo

642   (Addgene plasmid # 59776), (Kim et al., 2014)), referred to in the manuscript as

643   OptoFGFR, was subcloned in a lentiviral backbone for stable cell line generation.

644

Imaging

646   All acini images were acquired on an epifluorescence Eclipse Ti2 inverted

647   fluorescence microscope (Nikon) equipped with a CSU-W1 spinning disk confocal

648   system (Yokogawa) and a Plan Apo VC 60X water immersion objective (NA = 1.2).

649   For time lapse imaging, laser-based autofocus was used. Images were acquired with

650   a Prime 95B or a Prime BSI sCMOS camera (both Teledyne Photometrics) at 16-bit

651   depth. Temperature, CO_2 and humidity were controlled throughout live imaging with a

652   temperature control system and gas mixer (both Life Imaging Services).

653   All monolayer cell images were acquired on an epifluorescence Eclipse Ti inverted

654   fluorescence microscope (Nikon) with a Plan Apo 20x air objective (NA = 0.8) or a

655   Plan Apo 40X air objective (NA = 0.9). Laser-based autofocus was used throughout

656   imaging. Images were acquired with an Andor Zyla 4.2 plus camera at 16-bit depth.

657   Both microscopes were controlled by NIS elements (Nikon).

658

Inhibitors and growth factors

660   Gefitinib was obtained from Sigma-Aldrich/Merck and used at a concentration of 10

661   µM. Trametinib was obtained from Selleck Chemicals and used at a concentration of

662   5 µM. Batimastat was obtained from MedChem Express and used at a concentration

663   of 30 µM. Pictilisib was obtained from Selleck Chemicals and used at a concentration

664   of 250 nM. AZD5363 was obtained from Selleck Chemicals and used at a

665 concentration of 5 µM. IGF1 was obtained from Peprotech and used at a concentration
666 of 100 nM.

667

668 **Optogenetic experiments**

669 For short term optogenetics experiments performed directly on the microscope, acini
670 were illuminated with wide field blue light (470 nm LED) at defined time points during
671 spinning disc time lapse imaging. Acini expressing optoFGF were illuminated for 100
672 ms at 50% LED intensity. Acini expressing optoRAF were illuminated for 100 ms at
673 60% LED intensity. The NIS elements JOBS module was used to program the imaging
674 and stimulation patterns.

675 The 2D monolayer optogenetic experiments were executed by culturing MCF10A
676 expressing optoFGFR, ERK-KTR-mRuby2 and H2B-miRFP703 as confluent
677 monolayer on 24 well plates with glass bottom. Optogenetic stimulation was done with
678 488 nm LED light at 100% light intensity for 100ms and using a 20x air objective. To
679 generate larger ERK activity pulses, cells were stimulated with trains of 488 nm light
680 pulses with a 2 min interval. The area under the curve (AUC) of ERK activity was
681 calculated using the ERK activity levels before and after the ERK pulses to set the
682 baseline. The correlation function between the number of 488 nm light pulses and
683 AUC was obtained by linear regression. The effects of different frequencies with same
684 AUC on apoptosis was measured after 24 hours of time-lapse acquisition and manual
685 annotation of apoptotic events on the base of morphological alterations of cell nucleus.
686 For long term optogenetic stimulation with the LITOS system, glass bottom 96-well cell
687 culture plates with 7-day old acini were fitted on a 32 x 64 RGB LED matrix (Boxtec)
688 inside a cell culture incubator. The matrix was connected to a custom printed circuit
689 board with an ESP32 microcontroller. This system was programmed to emit 1-minute
690 blue light pulses at maximal intensity at defined intervals for 7 days, after which lumen
691 formation efficiency was assessed. Acini were fixed with 4% paraformaldehyde prior
692 to imaging.

693

694 **Image analysis of 3D acini**

695 The open source LEVERJS software (Cohen, 2014; Wait et al., 2014; Winter et al.,
696 2016) was used to analyze the 3D time lapse movies. The LEVERJS software was
697 updated to include improved processing and visualization capabilities. The processing
698 pipeline began with a GPU-accelerated 3D non-local means denoising algorithm (Wait

699 et al., 2019). After denoising, a new ensemble-based segmentation algorithm was
700 applied. This ensemble segmentation combined an adaptive thresholding into
701 foreground/background regions with an anisotropic 3D Laplacian of Gaussian filter
702 targeted to a specific cell radius to separate touching cells (Winter et al., 2019). The
703 base segmentation was run at different cell radii and the results were combined using
704 unsupervised learning techniques from the field of algorithmic information theory
705 (Cohen et al., 2009). Here, the radii evaluated ranged from 2.5 μm to 4 μm in 0.5 μm
706 steps. These values were set empirically based on expected cell size ranges.
707 Following segmentation, the cells were tracked using Multitemporal Association
708 Tracking (Winter et al., 2011); (Winter et al., 2012).

709 Following segmentation and tracking of the image sequences, the ERK-KTR signal
710 was extracted and processed to a detrended and normalized signal. To extract the
711 ERK-KTR signal, distance transforms were computed for each segmented image. The
712 interior distance transform assigned each cell interior voxel a numeric value indicating
713 its distance starting at the cell boundary and increasing to the centroid. The exterior
714 distance transform assigned each boundary voxel a numeric value indicating its
715 distance to the nearest cell-assigned voxel. The exterior distance transform also
716 provided the identity of the nearest cell-assigned voxel for each background voxel.
717 The ERK-KTR signal was computed as the ratio of the image values around the center
718 of the cell to the image values around the boundary of the cell. The center region of
719 the cell included voxels in the 95th percentile of the interior distance transform. For the
720 boundary region of the cell we included interior voxels within one unit of the boundary
721 and exterior voxels within three units of the boundary. The resulting ERK-KTR signal
722 was computed as the ratio of the median voxel value in the outer region to the median
723 voxel value in the inner region. The extracted ERK-KTR signals for each cell had
724 different base intensities and showed different amounts of fluctuation. To normalize
725 this and to allow for quantitative comparison and visual representation with different
726 cell ERK-KTR expression levels we computed a detrended and normalized ERK-KTR
727 signal as follows. The signal S was first detrended by subtracting the median filter
728 signal, $S_d = S - \text{median\_filter}(S)$. The signal was then normalized to the range [0,1]
729 using $S_{nd} = S_d / \max(S_d)$, unless the signal range in the detrended trajectory was below
730 an empirically set threshold. Inner and outer cells in stage 2 acini were identified
731 visually based on the 3D reconstructions in LEVERJS.

732 For segmentation and quantification of steady state Z-stacks, CellProfiler 3.1.8
733 (McQuin et al., 2018) with 3D functionalities was used. Nuclei were identified based
734 on H2B-miRFP signals. Apoptotic debris were identified using Caspase 3/7 Green
735 Detection kit signals using adaptive thresholding and watershed segmentation.
736 Geminin-mCherry intensities were measured within nuclei voxel masks. ERK-KTR
737 cytosolic/nuclear intensity ratios were generated by measuring median ERK-KTR
738 intensities in the nuclear area and in a spherical voxel mask 1 pixel around the nuclear
739 objects. Imaris software (Bitplane) was used for 3D rendering of confocal stacks and
740 to track and measure motility parameters in Figures 2 and 4.
741

Image analysis of 2D cell cultures

743 Nuclei of monolayer cells were segmented using Ilastik (Berg et al., 2019) and
744 CellProfiler 3.0. Ilastik was used for training a random forest classifier on different pixel
745 features of the H2B-miRFP channel and background pixels. The training data was
746 generated by manual annotation of 20 - 50 cells. The resulting probability map was
747 imported into CellProfiler for thresholding and segmentation. Cytosolic ERK-KTR
748 fluorescence intensities were measured by expansion of the nuclear objects. Cells
749 were tracked using μ-track 2.2.1 (Jaqaman et al., 2008).
750

Data analysis

752 All analysis and visualization of ERK activity peaks and time series was performed
753 with custom R/Matlab/Python code.

ERK activity pulse detection

755 ERK activity peaks were identified and counted by the following steps. 1. Application
756 of a short median filter to smooth the time series. 2. Application of a long median filter
757 to produce a bias estimate which was subtracted from the smoothed time series. 3.
758 Detrended time-series with real peaks were then identified by selecting those with an
759 activity difference above an empirical threshold. Those were rescaled to [0,1] and a
760 local maxima detection algorithm was used to identify peaks above an amplitude of
761 0.1.

Identification of collective events

763 To identify waves of collective ERK activation we developed a custom code and
764 implemented it in R. The algorithm works on a binarised signal that is calculated by

765   detrending and normalising ERK-KTR cytosolic/nuclear intensity ratio time series as

766   described above (Figure S3F,G). The algorithm searches for the first occurrence of

767   cells with ERK switched on (Figure S3H). If several such cells exist and they are

768   located within a threshold radius, they initiate the first collective event. A single active

769   cell can also become a collective event. In the next time point, the algorithm repeats

770   the search for active cells and compares their distances to cells in the previous frame.

771   If new active cells are located within the threshold distance to active cells at the

772   previous time point, they are added to respective collective events. If new active cells

773   are located outside of the threshold distance, they form new collective events. This

774   process of growing clusters of collective activity is repeated for all remaining time

775   points. The resulting statistics include the total number of cells involved in a collective

776   event, the duration and the average size of an event and the location (inner or outer

777   layer) of the cells that initiates the event.

778

779   **Immunoblotting and qPCR**

780   Cells were plated into 6-well dishes (2×10^5 cells/well) and cultured for 48h. The

781   resulting cell monolayers were washed twice with room temperature PBS, then

782   starving medium was added. For immunoblotting 1uL/mL DMSO or 10ug/mL

783   Batimastat was added together with the starving medium and cells were further

784   cultured for 72h. Media was removed, monolayers were washed twice with ice-cold

785   PBS, whole cell lysates were prepared and analyzed by immunoblotting as described

786   before (Dessauges et al., 2021). Primary antibodies against the following

787   proteins/epitopes were used: phospho-AKT^{Ser473} (cat. # 4058), AKT (cat. # 9272),

788   phospho-p44/42 MAPK (Erk1/2)$^{Thr202/Tyr204}$ (cat. # 4370), p44/42 MAPK (Erk1/2) (cat.

789   # 4695), all from Cell Signaling Technologies, BioConcept Ltd. Secondary

790   IRDye680LT- or IRDye800CW-conjugated anti-species specific IgGs were from LI-

791   COR. For qPCR cells were first starved for 24h, then fresh starving medium containing

792   1uL/mL DMSO or 2uM and 10uM pictilisib was added and cells were cultured for 24h.

793   Media was removed, monolayers were washed twice with ice-cold PBS, RNA was

794   isolated using TRIzol reagent. Reverse transcription was done with the ProtoScript II

795   reverse transcriptase kit (Bioconcept, M0368L). Real-time qPCR reactions were run

796   using the MESA Green qPCR MasterMix Plus for SYBR Green assay (Eurogenetec,

797   RT-SY2X-03+WOU) on the Rotor-Gen Q device (Qiagen). Each sample was tested in

798   triplicate. Expression of the gene of interest was calculated using the $2^{-\Delta\Delta Ct}$ method.

799 The sequences of the primer sets used are as follows: AREG, 5' -ACA TTT CCA TTC

800 TCT TGT CG- 3' (forward), and 5' - ACA TTT CCA TTC TCT TGT CG- 3' (reverse);

801 FLJ22101, 5' -TTC CCT GTG GCA CTT GAC ATT- 3' (forward), and 5'-CTT TTG CCT

802 CTG GCA GTA CTC A-3' (reverse).

803

Quantification and statistical analysis

805 All graphs were assembled and statistics were performed using R or Excel. Box plots

806 depict the median and the 25th and 75th percentiles; whiskers correspond to minimum

807 and maximum non-outlier values in Figures 1G, 2D, 3A, 3H, 3I, 5F, 6C, 6F, 7B, 7E,

808 S1C, S3B, S3C, S3D, S3E, S4B, S6A, S6B, S6C, S6D and S7A. Dot plots show

809 distribution of 50 randomly selected data points per condition, or all data points if there

810 are less than 50. Red lines in ERK activity trajectories represent the population

811 average. The statistical tests used and the significance thresholds are indicated in

812 each respective legend.

813

Data and code availability

815 The open-source code for LEVERJS is available at https://leverjs.net/git. All 3D

816 datasets that were analyzed with LEVERJS for this publication can be browsed

817 interactively at https://leverjs.net/mcf10a_3d.

818

827

Author contribution
829 PE, PAG and OP designed the study. PE, PAG and AF performed experiments and analyzed

830 data. MD and M-AJ analyzed data. CD provided expertise with the optogenetic tools. TH

831   provided expertise with LITOS. ARC performed image analysis using LEVERJS. PE, PAG and

832   OP wrote the paper.

833

Conflict of interest

835   The authors declare that they have no conflict of interest.

836

837

References

839   Aikin, T.J., Peterson, A.F., Pokrass, M.J., Clark, H.R., and Regot, S. (2020). MAPK activity

840   dynamics regulate non-cell autonomous effects of oncogene expression. ELife *9*.

841   Albeck, J.G., Mills, G.B., and Brugge, J.S. (2013). Frequency-modulated pulses of ERK

842   activity transmit quantitative proliferation signals. Mol. Cell *49*, 249–261.

843   Anderson, L.R., Sutherland, R.L., and Butt, A.J. (2010). BAG-1 overexpression attenuates

844   luminal apoptosis in MCF-10A mammary epithelial cells through enhanced RAF-1 activation.

845   Oncogene *29*, 527–538.

846   Aoki, K., Kumagai, Y., Sakurai, A., Komatsu, N., Fujita, Y., Shionyu, C., and Matsuda, M.

847   (2013). Stochastic ERK activation induced by noise and cell-to-cell propagation regulates cell

848   density-dependent proliferation. Mol. Cell *52*, 529–540.

849   Aoki, K., Kondo, Y., Naoki, H., Hiratsuka, T., Itoh, R.E., and Matsuda, M. (2017). Propagating

850   wave of ERK activation orients collective cell migration. Dev. Cell *43*, 305-317.e5.

851   Avraham, R., and Yarden, Y. (2011). Feedback regulation of EGFR signalling: decision

852   making by early and delayed loops. Nat. Rev. Mol. Cell Biol. *12*, 104–117.

853   Balasubramanian, S., Wurm, F.M., and Hacker, D.L. (2016). Multigene expression in stable

854   CHO cell pools generated with the piggyBac transposon system. Biotechnol. Prog. *32*, 1308–

855   1317.

856   Berglund, F.M., Weerasinghe, N.R., Davidson, L., Lim, J.C., Eickholt, B.J., and Leslie, N.R.

857   (2013). Disruption of epithelial architecture caused by loss of PTEN or by oncogenic mutant

858   p110α/PIK3CA but not by HER2 or mutant AKT1. Oncogene *32*, 4417–4426.

859   Berg, S., Kutra, D., Kroeger, T., Straehle, C.N., Kausler, B.X., Haubold, C., Schiegg, M., Ales,

860   J., Beier, T., Rudy, M., et al. (2019). ilastik: interactive machine learning for (bio)image

861   analysis. Nat. Methods *16*, 1226–1232.

862   Boocock, D., Hino, N., Ruzickova, N., Hirashima, T., and Hannezo, E. (2020). Theory of

863   mechanochemical patterning and optimal migration in cell monolayers. Nat. Phys.

864   Cancer Genome Atlas Network (2012). Comprehensive molecular portraits of human breast
865   tumours. Nature *490*, 61–70.

866   Chakrabarty, A., Rexer, B.N., Wang, S.E., Cook, R.S., Engelman, J.A., and Arteaga, C.L.
867   (2010). H1047R phosphatidylinositol 3-kinase mutant enhances HER2-mediated
868   transformation by heregulin production and activation of HER3. Oncogene *29*, 5193–5203.

869   Chen, N., Eritja, N., Lock, R., and Debnath, J. (2013). Autophagy restricts proliferation driven
870   by oncogenic phosphatidylinositol 3-kinase in three-dimensional culture. Oncogene *32*, 2543–
871   2554.

872   Ciarloni, L., Mallepell, S., and Brisken, C. (2007). Amphiregulin is an essential mediator of
873   estrogen receptor alpha function in mammary gland development. Proc Natl Acad Sci USA
874   *104*, 5455–5460.

875   Cohen, A.R. (2014). Extracting meaning from biological imaging data. Mol. Biol. Cell *25*, 3470–
876   3473.

877   Cohen, A.R., Bjornsson, C.S., Temple, S., Banker, G., and Roysam, B. (2009). Automatic
878   summarization of changes in biological image sequences using algorithmic information theory.
879   IEEE Trans. Pattern Anal. Mach. Intell. *31*, 1386–1403.

880   Debnath, J., Mills, K.R., Collins, N.L., Reginato, M.J., Muthuswamy, S.K., and Brugge, J.S.
881   (2002). The role of apoptosis in creating and maintaining luminal space within normal and
882   oncogene-expressing mammary acini. Cell *111*, 29–40.

883   Debnath, J., Muthuswamy, S.K., and Brugge, J.S. (2003). Morphogenesis and oncogenesis
884   of MCF-10A mammary epithelial acini grown in three-dimensional basement membrane
885   cultures. Methods *30*, 256–268.

886   Dessauges, C., Mikelson, J., Dobrzynski, M., Jacques, M.-A., Frismantiene, A., Gagliardi,
887   P.A., Khammash, M., and Pertz, O. (2021). Optogenetic actuator/biosensor circuits for large-
888   scale interrogation of ERK dynamics identify sources of MAPK signaling robustness. BioRxiv.

889   Du, W.W., Fang, L., Li, M., Yang, X., Liang, Y., Peng, C., Qian, W., O'Malley, Y.Q., Askeland,
890   R.W., Sugg, S.L., et al. (2013). MicroRNA miR-24 enhances tumor invasion and metastasis
891   by targeting PTPN9 and PTPRF to promote EGF signaling. J. Cell Sci. *126*, 1440–1453.

892   Fernández, P.A., Buchmann, B., Goychuk, A., Engelbrecht, L.K., Raich, M.K., Scheel, C.H.,
893   Frey, E., and Bausch, A.R. (2021). Surface-tension-induced budding drives alveologenesis in
894   human mammary gland organoids. Nat. Phys. *17*, 1130–1136.

895   Finlay, D., Healy, V., Furlong, F., O'Connell, F.C., Keon, N.K., and Martin, F. (2000). MAP
896   kinase pathway signalling is essential for extracellular matrix determined mammary epithelial
897   cell survival. Cell Death Differ. *7*, 302–313.

898   Gagliardi, P.A., Dobrzyński, M., Jacques, M.-A., Dessauges, C., Ender, P., Blum, Y., Hughes,
899   R.M., Cohen, A.R., and Pertz, O. (2021). Collective ERK/Akt activity waves orchestrate
900   epithelial homeostasis by driving apoptosis-induced survival. Dev. Cell *56*, 1712-1726.e6.

901   Gaiko-Shcherbak, A., Fabris, G., Dreissen, G., Merkel, R., Hoffmann, B., and Noetzel, E.
902   (2015). The acinar cage: basement membranes determine molecule exchange and
903   mechanical stability of human breast cell acini. PLoS ONE *10*, e0145174.

904

905   Gillies, T.E., Pargett, M., Minguet, M., Davies, A.E., and Albeck, J.G. (2017). Linear Integration
906   of ERK Activity Predominates over Persistence Detection in Fra-1 Regulation. Cell Syst. *5*,
907   549-563.e5.

908   Goedhart, J., von Stetten, D., Noirclerc-Savoye, M., Lelimousin, M., Joosen, L., Hink, M.A.,
909   van Weeren, L., Gadella, T.W.J., and Royant, A. (2012). Structure-guided evolution of cyan
910   fluorescent proteins towards a quantum yield of 93%. Nat. Commun. *3*, 751.

911   Goglia, A.G., Wilson, M.Z., Jena, S.G., Silbert, J., Basta, L.P., Devenport, D., and Toettcher,
912   J.E. (2020). A Live-Cell Screen for Altered Erk Dynamics Reveals Principles of Proliferative
913   Control. Cell Syst. *10*, 240-253.e6.

914   Gustin, J.P., Karakas, B., Weiss, M.B., Abukhdeir, A.M., Lauring, J., Garay, J.P., Cosgrove,
915   D., Tamaki, A., Konishi, H., Konishi, Y., et al. (2009). Knockin of mutant PIK3CA activates
916   multiple oncogenic pathways. Proc Natl Acad Sci USA *106*, 2835–2840.

917   Harada, H., Quearry, B., Ruiz-Vela, A., and Korsmeyer, S.J. (2004). Survival factor-induced
918   extracellular signal-regulated kinase phosphorylates BIM, inhibiting its association with BAX
919   and proapoptotic activity. Proc Natl Acad Sci USA *101*, 15313–15317.

920   Hino, N., Rossetti, L., Marín-Llauradó, A., Aoki, K., Trepat, X., Matsuda, M., and Hirashima,
921   T. (2020). ERK-Mediated Mechanochemical Waves Direct Collective Cell Polarization. Dev.
922   Cell *53*, 646-660.e8.

923   Hiratsuka, T., Fujita, Y., Naoki, H., Aoki, K., Kamioka, Y., and Matsuda, M. (2015). Intercellular
924   propagation of extracellular signal-regulated kinase activation revealed by in vivo imaging of
925   mouse skin. ELife *4*, e05178.

926   Höhener, T.C., Landolt, A., Dessauges, C., Gagliardi, P.A., and Pertz, O. (2022). LITOS - a
927   versatile LED illumination tool for optogenetic stimulation. BioRxiv.

928

929   Huang, C.Y., and Ferrell, J.E. (1996). Ultrasensitivity in the mitogen-activated protein kinase
930   cascade. Proc Natl Acad Sci USA *93*, 10078–10083.

931 Hubaud, A., and Pourquié, O. (2014). Signalling dynamics in vertebrate segmentation. Nat.
932 Rev. Mol. Cell Biol. *15*, 709–721.

933 Huebner, R.J., Neumann, N.M., and Ewald, A.J. (2016). Mammary epithelial tubes elongate
934 through MAPK-dependent coordination of cell migration. Development *143*, 983–993.

935 Inman, J.L., Robertson, C., Mott, J.D., and Bissell, M.J. (2015). Mammary gland development:
936 cell fate specification, stem cells and the microenvironment. Development *142*, 1028–1042.

937 Isakoff, S.J., Engelman, J.A., Irie, H.Y., Luo, J., Brachmann, S.M., Pearline, R.V., Cantley,
938 L.C., and Brugge, J.S. (2005). Breast cancer-associated PIK3CA mutations are oncogenic in
939 mammary epithelial cells. Cancer Res. *65*, 10992–11000.

940 Jaqaman, K., Loerke, D., Mettlen, M., Kuwata, H., Grinstein, S., Schmid, S.L., and Danuser,
941 G. (2008). Robust single-particle tracking in live-cell time-lapse sequences. Nat. Methods 5,
942 695–702.

943 Kholodenko, B.N., Hancock, J.F., and Kolch, W. (2010). Signalling ballet in space and time.
944 Nat. Rev. Mol. Cell Biol. *11*, 414–426.

945 Kim, N., Kim, J.M., Lee, M., Kim, C.Y., Chang, K.-Y., and Heo, W.D. (2014). Spatiotemporal
946 control of fibroblast growth factor receptor signals by blue light. Chem. Biol. *21*, 903–912.

947 Lam, A.J., St-Pierre, F., Gong, Y., Marshall, J.D., Cranfill, P.J., Baird, M.A., McKeown, M.R.,
948 Wiedenmann, J., Davidson, M.W., Schnitzer, M.J., et al. (2012). Improving FRET dynamic
949 range with bright green and red fluorescent proteins. Nat. Methods *9*, 1005–1012.

950 Lauring, J., Cosgrove, D.P., Fontana, S., Gustin, J.P., Konishi, H., Abukhdeir, A.M., Garay,
951 J.P., Mohseni, M., Wang, G.M., Higgins, M.J., et al. (2010). Knock in of the AKT1 E17K
952 mutation in human breast epithelial cells does not recapitulate oncogenic PIK3CA mutations.
953 Oncogene *29*, 2337–2345.

954 Lavoie, H., Gagnon, J., and Therrien, M. (2020). ERK signalling: a master regulator of cell
955 behaviour, life and fate. Nat. Rev. Mol. Cell Biol. *21*, 607–632.

956 Liu, J.S., Farlow, J.T., Paulson, A.K., Labarge, M.A., and Gartner, Z.J. (2012). Programmed
957 cell-to-cell variability in Ras activity triggers emergent behaviors during mammary epithelial
958 morphogenesis. Cell Rep. *2*, 1461–1470.

959 Mailleux, A.A., Overholtzer, M., Schmelzle, T., Bouillet, P., Strasser, A., and Brugge, J.S.
960 (2007). BIM regulates apoptosis during mammary ductal morphogenesis, and its absence
961 reveals alternative cell death mechanisms. Dev. Cell *12*, 221–234.

962 McQuin, C., Goodman, A., Chernyshev, V., Kamentsky, L., Cimini, B.A., Karhohs, K.W., Doan,
963 M., Ding, L., Rafelski, S.M., Thirstrup, D., et al. (2018). CellProfiler 3.0: Next-generation image

964   processing for biology. PLoS Biol. *16*, e2005970.

965   Myers, M.G., Sun, X.J., Cheatham, B., Jachna, B.R., Glasheen, E.M., Backer, J.M., and White,
966   M.F. (1993). IRS-1 is a common element in insulin and insulin-like growth factor-I signaling to
967   the phosphatidylinositol 3'-kinase. Endocrinology *132*, 1421–1430.

968   Paine, I.S., and Lewis, M.T. (2017). The Terminal End Bud: the Little Engine that Could. J.
969   Mammary Gland Biol. Neoplasia *22*, 93–108.

970   Patterson, K.I., Brummer, T., O'Brien, P.M., and Daly, R.J. (2009). Dual-specificity
971   phosphatases: critical regulators with diverse cellular targets. Biochem. J. *418*, 475–489.

972   Pearson, G.W., and Hunter, T. (2007). Real-time imaging reveals that noninvasive mammary
973   epithelial acini can contain motile cells. J. Cell Biol. *179*, 1555–1567.

974   Reginato, M.J., Mills, K.R., Becker, E.B.E., Lynch, D.K., Bonni, A., Muthuswamy, S.K., and
975   Brugge, J.S. (2005). Bim regulation of lumen formation in cultured mammary epithelial acini is
976   targeted by oncogenes. Mol. Cell. Biol. *25*, 4591–4601.

977   Regot, S., Hughey, J.J., Bajar, B.T., Carrasco, S., and Covert, M.W. (2014). High-sensitivity
978   measurements of multiple kinase activities in live single cells. Cell *157*, 1724–1734.

979   Sakaue-Sawano, A., Yo, M., Komatsu, N., Hiratsuka, T., Kogure, T., Hoshida, T., Goshima,
980   N., Matsuda, M., Miyoshi, H., and Miyawaki, A. (2017). Genetically encoded tools for optical
981   dissection of the mammalian cell cycle. Mol. Cell *68*, 626-640.e5.

982   Schafer, Z.T., Grassian, A.R., Song, L., Jiang, Z., Gerhart-Hines, Z., Irie, H.Y., Gao, S.,
983   Puigserver, P., and Brugge, J.S. (2009). Antioxidant and oncogene rescue of metabolic
984   defects caused by loss of matrix attachment. Nature *461*, 109–113.

985   Sebastian, J., Richards, R.G., Walker, M.P., Wiesen, J.F., Werb, Z., Derynck, R., Hom, Y.K.,
986   Cunha, G.R., and DiAugustine, R.P. (1998). Activation and function of the epidermal growth
987   factor receptor and erbB-2 during mammary gland morphogenesis. Cell Growth Differ. *9*, 777–
988   785.

989   Shaulian, E., and Karin, M. (2001). AP-1 in cell proliferation and survival. Oncogene *20*, 2390–
990   2400.

991   Shcherbakova, D.M., Baloban, M., Emelyanov, A.V., Brenowitz, M., Guo, P., and Verkhusha,
992   V.V. (2016). Bright monomeric near-infrared fluorescent proteins as tags and biosensors for
993   multiscale imaging. Nat. Commun. *7*, 12405.

994   Sparta, B., Pargett, M., Minguet, M., Distor, K., Bell, G., and Albeck, J.G. (2015). Receptor
995   Level Mechanisms Are Required for Epidermal Growth Factor (EGF)-stimulated Extracellular
996   Signal-regulated Kinase (ERK) Activity Pulses. J. Biol. Chem. *290*, 24784–24792.

997 Sternlicht, M.D., Sunnarborg, S.W., Kouros-Mehr, H., Yu, Y., Lee, D.C., and Werb, Z. (2005).
998 Mammary ductal morphogenesis requires paracrine activation of stromal EGFR via ADAM17-
999 dependent shedding of epithelial amphiregulin. Development *132*, 3923–3933.

1000 Tikoo, A., Roh, V., Montgomery, K.G., Ivetac, I., Waring, P., Pelzer, R., Hare, L., Shackleton,
1001 M., Humbert, P., and Phillips, W.A. (2012). Physiological levels of Pik3ca(H1047R) mutation
1002 in the mouse mammary gland results in ductal hyperplasia and formation of ERα-positive
1003 tumors. PLoS ONE *7*, e36924.

1004 Valon, L., Davidović, A., Levillayer, F., Villars, A., Chouly, M., Cerqueira-Campos, F., and
1005 Levayer, R. (2021). Robustness of epithelial sealing is an emerging property of local ERK
1006 feedback driven by cell elimination. Dev. Cell *56*, 1700-1711.e8.

1007 Wait, E., Winter, M., Bjornsson, C., Kokovay, E., Wang, Y., Goderie, S., Temple, S., and
1008 Cohen, A.R. (2014). Visualization and correction of automated segmentation, tracking and
1009 lineaging from 5-D stem cell image sequences. BMC Bioinformatics *15*, 328.

1010 Wait, E., Winter, M., and Cohen, A.R. (2019). Hydra image processor: 5-D GPU image
1011 analysis library with MATLAB and python wrappers. Bioinformatics *35*, 5393–5395.

1012 Wang, H., Lacoche, S., Huang, L., Xue, B., and Muthuswamy, S.K. (2013). Rotational motion
1013 during three-dimensional morphogenesis of mammary epithelial acini relates to laminin matrix
1014 assembly. Proc Natl Acad Sci USA *110*, 163–168.

1015 Winter, M.R., Fang, C., Banker, G., Roysam, B., and Cohen, A.R. (2012). Axonal transport
1016 analysis using Multitemporal Association Tracking. Int. J. Comput. Biol. Drug Des. *5*, 35–48.

1017 Winter, M., Wait, E., Roysam, B., Goderie, S.K., Ali, R.A.N., Kokovay, E., Temple, S., and
1018 Cohen, A.R. (2011). Vertebrate neural stem cell segmentation, tracking and lineaging with
1019 validation and editing. Nat. Protoc. *6*, 1942–1952.

1020 Winter, M., Mankowski, W., Wait, E., Temple, S., and Cohen, A.R. (2016). LEVER: software
1021 tools for segmentation, tracking and lineaging of proliferating cells. Bioinformatics *32*, 3530–
1022 3531.

1023 Winter, M., Mankowski, W., Wait, E., De La Hoz, E.C., Aguinaldo, A., and Cohen, A.R. (2019).
1024 Separating touching cells using pixel replicated elliptical shape models. IEEE Trans. Med.
1025 Imaging *38*, 883–893.

1026 Young, C.D., Zimmerman, L.J., Hoshino, D., Formisano, L., Hanker, A.B., Gatza, M.L.,
1027 Morrison, M.M., Moore, P.D., Whitwell, C.A., Dave, B., et al. (2015). Activating PIK3CA
1028 Mutations Induce an Epidermal Growth Factor Receptor (EGFR)/Extracellular Signal-
1029 regulated Kinase (ERK) Paracrine Signaling Axis in Basal-like Breast Cancer. Mol. Cell.
1030 Proteomics *14*, 1959–1976.

1031   Yusa, K., Zhou, L., Li, M.A., Bradley, A., and Craig, N.L. (2011). A hyperactive piggyBac
1032   transposase for mammalian applications. Proc Natl Acad Sci USA *108*, 1531–1536.